Pre-eruptive storage conditions and magmatic evolution of the Bora-Baricha-Tullu Moye volcanic system, Main Ethiopian Rift

A.Z. Tadesse[1*], K. Fontijn[1,2], L. Caricchi[3], F. Bégué[3], S. Gudbrandsson[4,5], V.C. Smith[6], P. Gopon[2,7], V. Debaille[1], P. Laha[8], H. Terryn[8], G. Yirgu[9], D. Ayalew[9]

[1]Department of Geosciences, Environment and Society, Université libre de Bruxelles (ULB), Belgium.

[2]Department of Earth Sciences, University of Oxford, UK.

[3]Department of Earth Sciences, University of Geneva (UNIGE), Switzerland.

[4]Reykjavik Geothermal Ltd, Iceland.

[5]TM Geothermal Operations PLC, Ethiopia.

[6]Research Laboratory for Archaeology and the History of Art, University of Oxford, UK.

[7]Department of Applied Geosciences and Geophysics, University of Leoben, Austria.

[8]Research Group of Electrochemical and Surface Engineering, Department of Materials and Chemistry, Vrije Universiteit Brussel (VUB), Belgium.

[9]School of Earth Sciences, Addis Ababa University (AAU), Ethiopia.

*Corresponding author: Address: 50 Av. F.D. Roosevelt, B-1050 Brussels, Belgium; Email: Amdemichael.Tadesse@ulb.be, amdemichaelz@gmail.com, Tel: +32471309363

Abstract

Bora-Baricha-Tullu Moye is a Late Quaternary volcanic system in the Main Ethiopian Rift, characterised by products of both explosive and effusive volcanic eruptions. The petrological and geochemical characteristics of the volcanic products are investigated using a combination of petrography, major and trace element whole rock analyses and in-situ major element analyses of phenocryst phases, matrix glass and melt inclusions. The bulk rock compositions vary from basalt to peralkaline rhyolite (comendite and pantellerite), and the chemical variability can largely be explained by fractional crystallisation processes with minor crustal assimilation and magma mixing. The dominant mineral phases such as clinopyroxenes and feldspars show a tendency for Fe and Na enrichment respectively from the basalts towards the pantellerites. The comendite and pantellerite deposits show systematic variations towards more evolved glass and mineral composition with the stratigraphy. The combination of thermometry (i.e., clinopyroxene-liquid, feldspar-liquid, olivine-liquid and clinopyroxene-only) and barometry (i.e., clinopyroxene-liquid and clinopyroxene-only) modelling suggests that the basaltic magmas are stored at high temperature (1070-1190 °C) at mid-to-deep-crustal levels (~7-29 km). The peralkaline rhyolite melts are stored at lower temperature (i.e., 805-900 °C for comendite; 700-765 °C for pantellerite) at shallow crustal levels (~4 km). The conditions of pre-eruptive storage as recorded in the comendite and pantellerite rocks in combination with stratigraphic constraints, suggests a progressive temporal evolution of the magma reservoirs to cooler storage temperatures.

Keywords: Main Ethiopian Rift, caldera system, magmatic evolution, pre-eruptive storage conditions, magmatic plumbing system

1. Introduction

In modern volcanology significant effort goes into linking monitoring signals observed at the surface of active volcanoes (e.g., seismicity, ground deformation and gas chemistry) with subsurface processes. As the depth at which these processes occur are inaccessible, magma storage depth, pre-eruptive temperature and magma volatile content, comes from studies of the eruptive products. Petrological methods have been broadly used to determine the magmatic storage conditions by analysing phenocryst and glass (melt inclusions and/or interstitial), from which saturation temperatures and pressures are calculated using phenocryst-liquid equilibrium reactions that are sensitive to the magmatic variables in question (e.g., Blundy and Cashman, 2008). Various thermobarometers, based on extensive experimental work and thermodynamic constraints, and calibrated for compositionally different igneous systems, were published over the last few decades and are widely used by the scientific community (e.g., Putirka et al., 1996; Putirka et al., 2007; Putirka, 2008; Blundy and Cashman, 2008; Neave and Putirka, 2017; Jorgenson et al., 2022).

The Main Ethiopian Rift (MER) is the volcanically active northern sector of the East African Rift that predominantly hosts silicic volcanic complexes, most of which have host large calderas (e.g. Corbetti, Shala, Aluto, Bora-Baricha-Tullu Moye (BBTM), Gedemsa, Boku, Boset, Kone and Fentale; Fig. 1). Within some of the big complexes, the eruption of basaltic magma along tectonically controlled fissures has emplaced variable proportions of lava flows and scoria cones (e.g. Corti, 2009, and references therein). Most MER silicic volcanoes experienced both effusive and explosive activity in their post-caldera stages (Martin-Jones et al., 2017; Fontijn et al., 2018; McNamara et al., 2018; Tadesse et al., 2022; Colby et al., 2022; Vidal et al., 2022). Some of those volcanoes (e.g., Corbetti, Aluto) are characterised as restless based on episodic to regular ground deformation (e.g., Biggs et al., 2011; Albino and Biggs, 2021; Hutchison et al., 2016a) or seismicity (e.g., Greenfield et al., 2019a, b).

Understanding the pre-eruptive magma conditions and tracking its evolution is vital in understanding the significance of volcano unrest and heat sources for volcano monitoring and geothermal energy exploration respectively. Magnetotelluric surveys have been used on some of the MER volcanoes (including at BBTM and Aluto) to better characterise the current geothermal reservoirs and magmatic plumbing systems (Hübert et al., 2018; Samrock et al., 2018, 2021). However, with the nature and resolution of these existing surveys, it remains challenging to identify crystal-rich (e.g., Hübert et al., 2018) or ephemeral reservoirs (Friðleifsson et al., 2014; Cashman et al., 2017; Edmonds et al., 2019), even in regions with dense instrument networks. The integration with petrography and geothermobarometry could therefore help constraining magmatic reservoir depth beneath active volcanoes.

In this study we present geochemical and petrological data to improve our understanding of the pre-eruptive storage conditions and magmatic evolution of BBTM, and of peralkaline rhyolite caldera-hosting volcanoes in general. We use natural mineral-liquid and whole rock compositions of representative samples that constrain the physical and chemical conditions of the magma before it erupted at the BBTM volcanic system. These data are used as input data for our thermobarometer modelling. Our constraints on the magmatic storage conditions at BBTM are integrated and compared with those from geophysical surveys.

2. Geological and geophysical setting

The MER is the northernmost part of the East African Rift that accommodates 4-6 mm/yr continental extension between the Nubian and Somalian Plates (e.g. Saria et al., 2014; Stamps et al., 2018). The MER is bordered by NE-SW oriented major faults, and an axial zone characterised by localised NNE-SSW faulting (Agostini et al., 2011). The axial zone is the focus of the Quaternary deformation and volcanism and hosts regularly spaced caldera-hosting volcanic complexes (e.g. Corbetti, Aluto, BBTM and Gedemsa; Fig. 1) and fault-controlled small eruptive centres (Ebinger and Casey, 2001; Keir et al., 2015). The whole-rock compositions of the MER magmas are commonly bimodal, with peralkaline trachytes and rhyolites dominating the large volcanoes and transitional to alkaline basalts erupting along the faults (e.g. Trua et al., 1999; Peccerilo et al., 2003; Ronga et al., 2010; Macdonald et al., 2012; Hutchison et al., 2016b; Tadesse et al., 2019).

The BBTM is one of the silicic volcanic systems located in the central sector of the MER (Fig. 1). Its volcanic history shows both effusive and explosive volcanism with one or more caldera forming eruptions; the most recent one of which occurred at 107.7 ± 8.8 ka (Tadesse et al., 2022). Since then, BBTM experienced at least one moderate-to-large explosive eruption (0.001 km^3 to 0.3 km^3 magma in dense rock equivalent, which corresponds to a magnitude of 2.5-4.8) per four thousand years (Tadesse et al., 2022). The geology of the BBTM is composed of volcanic products that mainly formed in the Late Quaternary (Di Paola, 1972; Abebe et al., 1998). Based on detailed field observations, petrography and geochemistry we modified the geological map of the BBTM that was previously presented by several authors (Di Paola, 1972; Bizouard and Di Paola, 1978; Abebe et al., 1998; Korme et al., 1999). The newly proposed surface geology of the BBTM comprises six main geological units (Fig. 1):

(1) Ignimbrite (Qni, 1.58 ± 0.2 Ma; WoldeGabriel et al., 1990): found in tectonically uplifted blocks east of the BBTM with a maximum thickness of 50 m. It is characterised by interbedded units of moderately welded greenish ignimbrites and unwelded pyroclastics. The moderately welded ignimbrites are composed of a fine-grained green matrix with highly altered dark fiamme and accessory rock fragments (Fig. 2a).

(2) Old Basalt (or Bofa Basalt, Qbb; 0.44-0.61 ± 0.05 Ma; Boccaletti et al., 1998): restricted to the NE and SE portion of the complex and with maximum thickness of 13-15 m (Fig. 1). It overlies the Ignimbrite in the foot of the eastern escarpment around Tullu Moye volcano

(Korme et al., 1999). These basalts are porphyritic in texture with predominantly plagioclase feldspar phenocrysts, and aphyric towards the top (Fig. 2b; Korme et al., 1999).

(3) Rhyolite / Trachyte Lava (Qrt): exposed in the centre and SW of the volcanic system and forming up to 40 m thick flow sheets or lava domes (e.g. Togee, Kurbeyu; Fig. 1). At the centre of the volcanic complex (Jima; Fig. 1) this unit is majorly affected by alteration which may result from persistent hydrothermal activity (Darge et al., 2019). Around Artu (N Tullu Moye) the flow of this unit overlies the Qbb (Korme et al., 1999). The Togee lava dome is made of feldspar-phyric rhyolite and contains significant basaltic rock xenoliths (Fig. 2e). The rhyolite at Kurbeyu is aphyric and shows flow banding.

(4) Rhyolite Pyroclastics (Qrp): monotonously covers the western part of the BBTM with multiple meters thick successions in some outcrops (Fontijn et al., 2018; Tadesse et al., 2022). It is composed of unwelded pumice flows, fall and ash alternations that sourced from caldera-forming eruptions (Suke and Meki), major post-caldera centres (i.e., Bora, Baricha, Tullu Moye), small edifices (e.g. Oda, Werdi; Fig. 2c) and localised pumice cones (Tadesse et al., 2022). The youngest caldera-forming event occurred at 107.7 ± 8.8 ka, and above its deposits, multiple deposit sequences, alternating with palaeosols, representing individual eruptions are recognised. A minimum of 25 such post-caldera eruptions are identified in the BBTM, sourced from the Baricha (9 events), Oda (8), Bora (3), Werdi (3) and Tullu Moye (2) volcanic centres (Tadesse et al., 2022). In the eastern sector of the volcanic complex the rhyolite tephra is intercalated with black scoria layers (MER373; SI-1); in others there is a gradual enrichment of scoria clasts up through the stratigraphy (MER251; Fig. 2d).

(5) Young Basalts (Qwb; Wonji Basalt; WoldeGabriel et al., 1990): exposed as patches that cover the highly faulted portion of the BBTM. This unit is associated with scoria and spatter cones (Fig. 2b) that are aligned along NNE-SSW trending tensional fissures. The Qwb lava

flows cover the gentle slopes of the Rhyolite Pyroclastics (Qrp) or Rhyolite / Trachyte Lava (Qrt). In contrast to the Old Basalt, the Young Basalt Lava is predominantly aphyric.

(6) Obsidian Coulees (Qoc): were extruded along the same fissures as the mafic cones in the east. They emanate from different NNE-SSW aligned vents and form semi-circular, elliptical or, rarely, elongated domes and ridges with 1.6 km^2 to 18.9 km^2 areal coverage. The two youngest and least vegetated lavas (Giano=15 km^2, Gnaro=18.9 km^2; Fig. 1) are also the largest in the complex, and comprise >5 m thick lobes. Most obsidian flows are banded and display well preserved to highly fractured flow folding (Fig. 2f).

The oldest geological units (i.e. Qni, Qbb) are considered to pre-date the BBTM complex and to be associated to the still poorly understood regional volcanism that emplaced the Nazret and Bofa units during late Miocene to early Pleistocene (WoldeGabriel et al., 1990; Boccaletti et al., 1998; Tadesse et al., 2022). The BBTM-related volcanism thus only encompasses the Rhyolite / Trachyte Lava (Qrt), Rhyolite Pyroclastics (Qrp), Young Basalts (Qwb) and Obsidian Coulees (Qoc) that are distributed around the volcanic complex. At lower elevations, the central and southern portions of the volcanic system are covered by lacustrine and alluvial deposits (Abebe et al., 1998).

BBTM is considered as an active volcanic system in the MER with ongoing seismicity (Greenfield et al., 2019a, b) and surface deformation (Biggs et al., 2011; Albino and Biggs, 2021). InSAR observations spanning the periods of 2004 - 2010 (Biggs et al., 2011) and 2015 - 2020 (Albino and Biggs, 2021) show long-term active ground deformation. Two pulses of uplift alternating with subsidence were observed in 2004 and 2008 to 2010 (each ~2 cm/yr uplift), and were attributed to a shallow (<2.5 km) penny-shaped crack source under BBTM (Biggs et al., 2011). Albino and Biggs (2021) recently observed new episodes of deformation located between the three volcanic edifices of Bora, Baricha and Tullu Moye, suggesting ca. 5.8 cm/yr uplift in early 2016. The ground deformation rate then exponentially decreases to

1.9 cm/yr for the period 2017-2020. The deformation signals are consistent with migration of fluids under BBTM (Albino and Biggs, 2021). The seismicity catalogue of Greenfield et al. (2019a, b) shows clustering of small magnitude earthquakes around Tullu Moye, Bora and a region between these two volcanic edifices. The seismicity predominantly occurs as volcano-tectonic and low-frequency earthquakes, the latter sourced from fluid circulation along pre-existing fractures (Greenfield et al., 2019a, b). Additionally, magnetotelluric data shows two electrically conductive zones beneath the BBTM in the lower (14 km) and upper (4 km) crust, the latter distinctly located underneath the Tullu Moye edifice (Samrock et al., 2018, 2021). A high conductivity region at more shallow depth is interpreted as the result of enrichment of conductive smectite clays formed by convective hydrothermal alteration (“clay cap”).

3. Methodology

The rock samples used in this study were collected during four different field campaigns between 2015 and 2020, and span a range of compositions and sampling sites, covering the entire complex.

A total of 98 samples were selected for whole rock analysis. The selected samples represent the entire range of the volcanism in BBTM; in terms of stratigraphy, spatial distribution and chemical composition (SI-1). Samples were trimmed to obtain the freshest portions, which were then crushed and milled in an agate ball mill to produce powders. Loss on ignition (LOI) was determined after ignition for 1 hour at 850 °C (silicic) and 950 °C (mafic) on dried sample powders. Whole-rock major and trace element compositions were acquired by Inductively Coupled Plasma Optical Emission Spectrometry (ICP-OES) using a Thermofischer Scientific iCAP and by Inductively Coupled Plasma Mass Spectrometry (ICP-MS) using a Quadrupole ICP-MS Agilent 7700 respectively, at the Laboratoire G-TIME of the Université libre de Bruxelles. The analyses were performed on samples after powdering, alkaline fusion using a 1:1 mixture of lithium tetra- and metaborate, and dilution by HNO_3.

Precision of <5% for major elements and <10% for trace elements was achieved using calibration curves made of synthetic standards, internal standard (In for ICP-MS and Y for ICP-OES) and a range of geological standards. The entire data set, including geographic coordinates and respective geological and stratigraphic units of each sample, is presented in the Supplementary Information (SI-1).

Thin sections and grain mounts on selected samples were used for petrographic and geochemical analysis. Thin sections and glass grain mounts were prepared as per Tadesse et al. (2022). To prepare crystal grain mounts, fresh pumice clasts were manually crushed using an agate pestle and mortar. The crushed samples were dry-sieved at 1ϕ intervals between -1ϕ (2 mm) and 2ϕ (0.25 mm) and crystals were manually picked under a stereomicroscope. The recovered mineral grains were cold-mounted in EpoFix resin rings. Separate grain mounts were prepared for each mineral type (e.g., feldspars, Fe-Ti oxides), and ground with SiC paper (grade P800, P2400) and finally polished with diamond paste (3 and 1 micron).

Prior to Electron Microprobe Analysis (EPMA), phenocrysts were inspected with a JEOL JSM-IT300 scanning electron microscope fitted with backscattered electron and Oxford instruments X-MaxM energy dispersive X-ray detectors, at the Department of Materials and Chemistry, Vrije Universiteit Brussel, to verify the unaltered nature of the mineral phases (e.g., to distinguish aenigmatite from amphibole) and to identify the presence of exposed melt inclusions. Phenocryst phase and melt inclusion major element data were acquired by EPMA using a CAMECA SX5-FE and JEOL JXA-8200 at the Departments of Earth Sciences at the University of Oxford and University of Geneva respectively. Analytical conditions, reference material and protocols were the same on both instruments, and some samples were analysed on both instruments to evaluate reproducibility. Carbon-coated well-polished samples were analysed at 15 kV accelerating voltage. We used a focused beam and 20 nA beam current for the analysis of aenigmatite, pyroxene, olivine and Fe-Ti oxides. A defocused beam was applied for the analysis of amphibole and feldspar (5 µm; 15 nA), and melt inclusions (5 µm; 10 nA). Peak and background counting times were set respectively to 30 and 15s (Si, Al, Ti, Ca, S, Cl), 50 and 25s (F) and 60 and 30s (P, Mg, Mn, Fe). To reduce alkali migration, Na and K were analysed first with 20s peak and 10s background counting times in all the mineral phases. Additionally, volatile species (F, Cl and S) were also measured first along with the alkalis in melt inclusions. For each quantified element, internal calibration standards of different appropriate minerals were used. For glass analysis, StHs6/80-G and ATHO-G standards (Jochum et al., 2006) were used as reference material. In each mineral grain, both core and rim, or transects were targeted to capture any chemical variability if present. The full data set is presented in the Supplementary Information (SI-2: glass; SI-3: minerals).

4. Results

4.1. Petrography

The BBTM rhyolite and trachyte lavas of unit Qrt are microcrystalline to sparsely glomerophyric (Fig. 3a). The silicic lava at Kurbeyu is made of microcrystalline alkali feldspar and quartz, whereas lavas from Togee and Jima, two domes in the centre of the volcanic complex (Fig. 1), are glomerophyric to holohyaline. The main macrocryst phases (>0.5 mm) are alkali feldspar with subordinate quartz, aenigmatite and orthopyroxene that together represent up to ca. 20 vol.%. Intergrowth of alkali feldspar and quartz is common in the glomerophyric rhyolites. The Togee lava has ca. 15 vol.% alkali feldspar that characterised by half sector zoning. It also contains mm-size (35 mm) mafic rock nodules with partially resorbed xenocrysts of plagioclase feldspar, Fe-Ti oxide and orthopyroxene in a microcrystalline matrix (Fig. 3a).

Basalt and scoria in the BBTM are predominantly vesicular and microcrystalline (Fig. 3b). The mineral phases are mainly plagioclase feldspar, clinopyroxene, olivine, orthopyroxene and Fe-Ti oxides. The olivine crystals in the basalt and scoria from unit Qwb are relatively coarse (>0.3 mm) and show a resorbed habitus. The Old Basalt (Qbb) is hypocrystalline with 20-35 vol.% phenocrysts (Fig. 3c). The plagioclase feldspar in the Qbb typically has oscillatory zoning and sieve textures (Fig. 3c), which is not observed in the Young Basalt of Qwb. In both units, Old and Young basalts, it is common to find olivine and clinopyroxene inclusions in plagioclase feldspar.

Rhyolite Pyroclastics (Qrp) are vesicular and holohyaline (Fig. 3d). The vesicles take up a high proportion of the volume (up to 75 vol.%) and the vesicle shape varies from sub-spherical to elongated polylobate with the longest dimensions of maximum 3 mm measured in thin section. There are few macrocrysts (<10 vol.%). The mineral phases are dominated by alkali feldspar, with subordinate aenigmatite, quartz, clinopyroxene, orthopyroxene and amphibole. The alkali feldspar and clinopyroxene macrocrysts host inclusions of apatite (max. 50 μm), and Fe-Ti oxides (in Tullu Moye; Fig. 3e). The Tullu Moye tephra has no aenigmatite and amphibole in the mineral assemblage. The tephra exposed in section MER251 has a clear variation in mineral assemblage along the stratigraphy, from aenigmatite and alkali feldspar at the bottom to clinopyroxene and plagioclase feldspar dominated at the top.

Obsidian of the BBTM is glomerophyric, with up to 10 vol.% macrocryst aggregates in a glassy matrix (Fig. 3f). The glomerocryst assemblage contains macrocrysts of alkali feldspar, aenigmatite, orthopyroxene, clinopyroxene, quartz and rare amphibole. Flow bands in the obsidian are characterised by variations from dark to pale yellow matrix colours (Fig. 3f). The Giano obsidian preserves well aligned alkali feldspar, clinopyroxene and small elliptical vesicles (<3 mm in their longest dimension) along the flow bands.

Some mineral phases in the Rhyolite Pyroclastics, predominantly clinopyroxene, aenigmatite and amphibole, contain naturally quenched melt inclusions in various proportions. Their size ranges from 10 to 300 μm and their shape is highly elongated to sub-spherical. They are usually completely glassy, without any post-entrapment crystallization or shrinkage bubble, and most of them are fully enclosed in the host mineral (Fig. 3e). Only few melt inclusions in amphibole show a connection to the matrix along the mineral cleavage direction and have apparent spherical bubbles in larger (> 20 µm) melt inclusions.

4.2. Whole rock chemistry

Major elements

Loss of Ignition (LOI) values vary from 0 to 7 wt%, with the higher values (>3 wt%) only observed in pyroclastic rocks. Since some of these high-LOI samples also show a significant drop in Na_2O (ca. 2.7 wt%) compared to those with low-LOI, the higher values are likely attributed to post-depositional alteration (e.g., Fontijn et al., 2013; Tadesse et al., 2019). All data were normalised to 100% before plotting and interpretation.

The BBTM major element data show a bimodal composition on the Total Alkali-Silica (TAS) classification diagram (Le Bas et al., 1986) with very few samples plotting in the 52 - 70 wt% SiO_2 range (Fig. 4a; Le Bas et al., 1986), which has also been observed for other MER volcanic systems (e.g. Peccerillo et al., 2003; Giordano et al., 2014; Hutchison et al., 2016b; Tadesse et al., 2019). The two compositional end members mainly fall into the basalt (47.3 - 52 wt% SiO_2; 3.9 – 6.6 wt% MgO) and rhyolite fields (70 - 77.1 wt% SiO_2; <0.8 wt% MgO). Few samples (e.g., MER373, MER251) plot in the intermediate range on the TAS diagram. The basaltic rocks are mildly alkaline (Fig. 4a) and most are dominated by hypersthene-olivine (transitional basalt, n=12) in their CIPW norm, with some nepheline-olivine (alkaline basalt, n=6) normative ones. The silicic volcanic products have a peralkaline rhyolite composition with peralkalinity index (PI = mol $[Na_2O+K_2O]/Al_2O_3$) ≥1. A few silicic pyroclastic samples with LOI >5 wt% frequently have a lower PI (0.6 – 0.9) due to alteration-induced depletion in some mobile major elements. The peralkaline rhyolite classification (after Macdonald, 1974) shows three main compositional fields: pantellerite (5.1 - 8.4 wt% FeO), comendite (2.2 - 5.5 wt% FeO) and comenditic trachyte (4.2 – 5.9 wt% FeO; Fig. 4b). The volcanic products from the caldera-forming eruptions (Meki, Suke), Baricha, Bora, Oda, Werdi, pumice cones and Kurbeyu are pantelleritic in composition. Most of these pantelleritic samples fall near the pantellerite-comendite dividing line and have a slightly higher Al_2O_3 content (9.8 – 12.4 wt%). Only Baricha pyroclastic samples have lower Al_2O_3 contents (8.8 – 10.6 wt%) and plot firmly in the pantelleritic field. Tullu Moye rhyolitic pyroclastic samples, obsidian coulees and the Togee rhyolite lava all have a comendite composition. Rare comenditic trachyte samples are from the Salen range and interbedded pumice-scoria deposits at section MER251.

Bivariate plots with SiO_2 as a differentiation index show two different trends (Fig. 5, SI-4-1). TiO_2, MgO, FeO, CaO and P_2O_5 show a negative correlation with SiO_2 from the mafic to the silicic compositions. P_2O_5 has relatively gentle slope and a positive trend in the mafic composition range. The K_2O, and to a lesser degree Na_2O after ca. 70 wt% SiO_2, contents increase with SiO_2, with a pronounced decrease in Na_2O. The Al_2O_3 against SiO_2 has a bimodal trend with nearly no variation up to 68.8 wt% SiO_2 followed by an immediate decrease of Al_2O_3 from 15.1 to 8.5 wt% within the silicic rocks.

Trace elements

The whole rock trace element data of the BBTM rocks display a wide compositional range just like the major element data. The Zr content varies strongly from the mafic (99 – 290 ppm) to the silicic rocks (391 – 1812 ppm), with slight variations between comenditic trachyte (432 – 570 ppm), comendite (391 – 965 ppm) and pantellerite (658 – 1812 ppm) samples. For this reason, Zr is used as a differentiation index on the trace element binary plots (Fig. 6 and SI-4). The compositional gap in Zr between the mafic and silicic rocks is narrower (290 – 390 ppm Zr) than is observed in SiO_2 on the major element plots. The incompatible trace elements (e.g. Y, La) show a positive correlation with Zr (Fig. 6). There is a slight dispersion in some incompatible elements within the felsic rocks which is also apparent on some trace element ratios (eg. Rb/Nb: 0.6 – 2.3; Th/Ta: 0.02 – 2.7; Ba/Nb: 0.2 – 12.6). Compatible trace elements (e.g. Sr) show a negative correlation with the differentiation index. Barium first shows a positive correlation with Zr up to the comenditic trachyte samples, and then a sharp decrease in the comendite and pantellerite compositions.

REE and multi-element spider diagrams are plotted on Fig. 7, and normalised to chondrite (after Boynton, 1984) and primordial mantle (after McDonough and Sun, 1995) compositions respectively. The mafic and felsic rocks have similar general patterns in both plots with generally higher elemental concentrations in the pantelleritic rhyolites. Both mafic and silicic rocks are enriched in LREE relative to HREE (La_N/Yb_N=6-14). The Eu anomaly is less pronounced or absent in the mafic compositions (Eu/Eu*=0.9-1.2) relative to the silicic ones (Eu/Eu*=0.3-0.8). Both the Togee rhyolite sample (Eu/Eu*=0.07), and sample MER243A (Eu/Eu*=0.6) within the mafic suite show more pronounced negative Eu anomalies. The spider diagrams show major positive spikes in Ta, and minor positive and negative peaks in a few other trace elements (Ba, U, Pb, Nd). In the silicic samples, the pantelleritic rocks have a trough in Ba, Sr and Ti, whereas the comenditic rocks have negative anomalies in P and Ti only.

4.3. Matrix glass and melt inclusion chemistry

Glass major element compositions were analysed on pristine glass across the entire compositional range of our samples. The data on the silicic and mafic samples presented here (SI-2) complements the already published glass composition data set of silicic samples (Fontijn et al., 2018; Tadesse et al., 2022). The glass compositions generally overlap with the whole rock compositions, which may be related to the generally crystal-poor nature of the BBTM rocks (Fig. 5). Only some oxides such as K_2O and P_2O_5 are slightly enriched in the glass of the mafic samples relative to their bulk composition. The glass thus exhibits a similar chemical variability than the whole rock, i.e. basalt, comendite and pantellerite. Scoria cones in the eastern part of BBTM (Fig. 1) have basaltic glass compositions (Fig. 4). One scoria cone located 2 km east of the Togee lava dome has a basaltic trachy-andesite/trachy-andesite composition (54.8-57.1 wt% SiO_2). The interbedded scoria and pumice deposits near the Oda crater (Fig. 2d) show a change in glass composition of the scoria up through the stratigraphy, from more silicic at the bottom (68.5 - 69.9 wt% SiO_2) to more mafic at the top (50.8-52.4 wt% SiO_2). The comendite population of Tullu Moye samples shows two distinct clusters representing the younger TM-P2 and older TM-P1 pumice units (Tadesse et al., 2022). This chemical distinction between Tullu Moye units is not visible in the whole rock data. The pantelleritic field is represented by the homogeneous highly evolved compositions of the caldera-forming eruptions (Suke, Meki), and the Baricha, Bora, Oda and Werdi pyroclastic products.

Melt inclusions are hosted in pyroxene, aenigmatite and amphibole macrocrysts in the silicic pyroclastics. The analysed melt inclusions are mainly of high-silica rhyolite composition, with SiO_2 contents ranging from 70 to 75.5 wt% (Fig. 8). A few melt inclusions in clinopyroxene and amphibole are dacitic to trachytic with 60.6 to 69 wt% SiO_2 (Fig. 4). The melt inclusions in the clinopyroxene are predominantly enriched in Al_2O_3 (>12 wt%; Fig. 8) compared to those in the amphibole and aenigmatite. Similar to the groundmass glass, the melt inclusion compositions also overlap with the whole rock compositions (Fig. 4, 5).

Some volatile elements (F, Cl, S) were quantitatively analysed in the melt inclusions, and the approximate water content was estimated using the water-by-difference method (e.g., Hughes et al., 2019). The volatile content is systematically higher in the melt inclusions than in the groundmass glass (<0.2 wt% of Cl, F and S). The analysed contents range from 0.07 - 0.5 wt% Cl, below detection limit - 0.3 wt% F and below detection limits - 0.08 wt% S. Melt inclusions in the comenditic and pantelleritic samples have H_2O_{diff} (assuming difference from 100% H_2O) ranging from 0.6 to 4.5 wt% (Fig. 8), with a few (n=3) anomalously high values (6.6-8.8 wt% H_2O_{diff}) for some melt inclusions in clinopyroxene and amphibole. The melt inclusion host minerals' cleavage may cause volatile diffusive loss. However, the H_2O_{diff} estimates obtained here are comparable to the measured H_2O (<2 to 8 wt%) contents by secondary ion mass spectrometry (SIMS) in quartz-hosted melt inclusions of Fentale and Corbetti lavas and pyroclastics, and which also have relatively low CO_2 content (100-300 ppm; Iddon and Edmonds, 2020).

4.4. Mineral chemistry

The mineralogical assemblage shows some variation as a function of the whole rock composition. Feldspar (plagioclase and/or alkali feldspar) and clinopyroxene coexist in all BBTM rocks. Other mineral phases such as orthopyroxene, aenigmatite, amphibole, olivine and Fe-Ti oxides are only present in specific compositions (Section 4.1). The full dataset of the mineral chemistry and plots for the subordinate mineral phases (i.e., Fe-Ti oxides) are provided in Supplementary Information (SI-3, SI-4). The classification of feldspar, pyroxene and amphibole macrocryst compositions are summarised in Figure 9, and histograms and compositional profiles are provided in Figures 10 and 11, respectively.

Feldspar

Plagioclase feldspar occurs as subhedral macrocrysts (max. 2 mm) in basaltic and comenditic rocks. In the comendite, the plagioclase is only identified in Tullu Moye older pumice (TM-P1). The plagioclase takes up 2 to 13 vol% of the modal proportion in both basalts and comendites, with the smallest proportions in the pyroclastic deposits. In the basaltic rocks the compositional variation ranges from bytownite to labradorite (An_{56-85}), while in the comendites it varies from labradorite to oligoclase (An_{18-58}; Fig. 9a, 10). In neither rock types, there are any systematic differences between core and rim, indicating equilibrium crystallisation (Fig. 10a, SI-4-5a).

Alkali feldspar occurs in the comenditic (i.e. younger pumice, TM-P2) and pantelleritic products. The macrocrysts are subhedral to euhedral, have a maximum crystal size of 1.2 mm, and represent 0.2 to 15 vol.% of the modal proportion. The general composition is anorthoclase in the comendites (Or_{19-27}; Fig. 9a), and sanidine in the pantellerites (Or_{19-52}). Those in the Baricha deposits have a distinct, more Or-rich, sanidine composition (Or_{40-52}; Fig.9a) than the other pantellerites. The alkali feldspars rim and core analyses indicate no significant variation in either rock type (Fig. 10b).

Pyroxene

Clinopyroxene occurs in all analysed rocks as subhedral to euhedral crystals up to 0.5 mm in size. The volumetric proportion of pyroxene phenocrysts are ranges from 0.2 to 5%. Clinopyroxene and orthopyroxene formula calculations were made considering stoichiometric Fe^{3+}/Fe^{2+} ratios following Droop (1987). The clinopyroxene composition primarily falls on the diopside-augite-hedenbergite boundary, following the nomenclature of Morimoto et al. (1988) (Fig. 9b). Clinopyroxene in the basalts is mainly diopside (Wo_{37-47}, En_{35-45}, Fs_{13-18}), while the clinopyroxene in the comendites shows two compositional clusters, i.e. augite-hedenbergite (Wo_{41-44}, En_{35-44}, Fs_{14-23}) for the older Tullu Moye pumice TM-P1, and augite (Wo_{39-44}, En_{15-38}, Fs_{22-44}) for the younger Tullu Moye TM-P2 (Fig. 9b). The pantellerite-hosted clinopyroxenes are also augites, but extremely rich in Fe (Wo_{40-42}, $En_{0.7-1}$, Fs_{57-59}). The Mg# and Al contents of the clinopyroxene in the basalt (70 ± 3 Mg#; 0.2 ± 0.07 apfu Al) and comendite (TM-P1: 70 ± 3 Mg#; 0.05 ± 0.03 apfu Al; and TM-P2: 40 ± 10 Mg#; 0.02 ± 0.005 apfu Al) are strikingly different. The clinopyroxene crystals from TM-P2 and the basalts show reverse zoning with Al-Ti-Fe-rich cores, while those in the pantellerites and TM-P1 are homogeneous (Fig. 10d and 11d). High-resolution single-crystal compositional profiles from core to rim on these zoned crystals indicate variations in Mg# (e.g. ± 5 Mg# in TM-P2; Fig. 11e). Few clinopyroxene crystals in the basalts display normal zoning and have Al-Ti- and Fe-rich rims.

Orthopyroxene occurs in pantelleritic and comenditic eruptive products in small proportions (<4%). The orthopyroxenes are classified as enstatite (En_{50-76}; Fig. 9b), with the more Mg-rich ones (En_{63-76}) in the pantellerites. Within the comendites, TM-P1 orthopyroxene is also slightly more Mg-rich (En_{54-64}) than that of the younger TM-P2 (En_{50-58}). Orthopyroxene crystals in the pantellerite show heterogeneity, which is reflected in their significant cation content variation between core and rim (e.g. ± 10% Mg#; Fig. 10c, 11b). The orthopyroxene crystals in the comendites do not show any significant systematic compositional variation between the core and rim (Fig. 11d).

Others

Aenigmatite and amphibole are found only in pantelleritic BBTM rocks in subordinate proportions (<3 vol%). They both have a black colour and acicular crystal habits but can be distinguished by petrographic microscope. Within the pantellerite the composition of the aenigmatite shows a slight variation between the Meki (2 ± 0.02 apfu Ti; 0.2 ± 0.02 apfu Ca) and Baricha deposits (1.8 ± 0.03 apfu Ti; 0.1 ± 0.05 apfu Ca; Fig. 10e). Amphiboles are only identified in the Baricha deposits and are Mg-poor (4 ± 2% Mg#; Fig. 10f). They are classified as Na-Ca (richterite and katophorite) and Na (eckermannite) amphiboles, following the Hawthorne et al. (2012) nomenclature (Fig. 9c-d). Core and rim analyses in both aenigmatite and amphibole indicate essentially homogeneous chemistry. A high-resolution compositional profile of an amphibole however shows a minor gradual increase in Mg# from core to rim (± 1% Mg#; Fig. 11a-b).

Fe-Ti oxides occur predominantly as glomerocryst clots and microlites in comenditic and basaltic rocks. A few crystals are also identified as inclusions in feldspar and clinopyroxene from Tullu Moye deposits. The Fe-Ti oxides in basaltic rocks are predominantly physically attached to plagioclase feldspar and clinopyroxene. All the Fe-Ti oxides are titano-magnetite plotting along the ulvöspinel-magnetite series (Fig. SI-5-4). The Fe-Ti oxides in the basalts are close to ulvöspinel whereas in the comendite they gradually progress to the magnetite side. The titano-magnetite in comendite shows two distinct compositional modes, with those from TM-P2 relatively enriched in Ti and Fe^{2+} compared to TM-P1.

Olivine is present only in basaltic rocks, showing variable crystal habits. Some olivine crystals are included in plagioclase feldspar; however, more commonly they occur as single euhedral to anhedral grains. The anhedral olivine from scoria deposits shows resorbed textures and rounded shapes. Compositionally, the olivine is relatively Mg-rich but highly heterogeneous, with forsterite contents ranging from Fo_{50} to Fo_{84} (Fig.10g). The analysed scoria cone sample is predominantly made of Mg-rich olivine compared to the basaltic lava flows (Fig. 10g). The core and rim compositions of the olivines in the lava flows show both normal and reverse zoning (Fig. 10g).

4.5. Geothermobarometry

Geothermobarometry calculations are performed on BBTM volcanic samples to capture the pre-eruptive storage conditions (P-T) and magmatic evolution within the crust. Clinopyroxene (cpx), orthopyroxene (opx), feldspar (fsp) and olivine (ol) were paired to putative equilibrium liquid (liq) compositions or each other to retrieve temperature and pressure. Only mineral analyses which fall within the expected stoichiometric total ± 0.05 apfu are considered for the thermobarometer estimations. The liquid components used were clinopyroxene-hosted melt inclusions and interstitial glass compositions that were checked for chemical equilibrium using the criteria discussed in Putirka (2008). Exceptionally, we considered whole rock chemistry as a liquid composition for one microcrystalline, moderately phyric (10 vol%) basaltic sample (MER335) due to the absence of interstitial glass or melt inclusions.

The thermobarometer models were selected based on their best performance composition, temperature and pressure range (Putirka, 2008 and references therein). The thermobarometers' performance was checked by their ability to recover experimental conditions of isothermal, isobaric phase equilibrium experiments of Putirka et al. (1996), Scaillet and Macdonald (2003) and Romano et al., (2020). Putirka et al. (1996) use ankaramite from Mauna Kea as a starting composition, a material with alkaline affinity similar to BBTM basalts. Experiments by Scaillet and Macdonald (2003) were conducted on phenocryst-poor comenditic obsidian, while Romano et al. (2020) used pantellerite samples. The latter two experiments together cover the entire range of observed BBTM peralkaline rock compositions. The testing result of the applied thermobarometers' performance is reported in the supplementary files (SI-5).

The storage temperatures for the basaltic suites are estimated using cpx-liq (Putirka et al., 1996; Neave and Putirka, 2017; Jorgenson et al., 2022), ol-liq (Putirka et al., 2007) and fsp-liq (Putirka, 2008) thermometers. The silicic suites' (comendite and pantellerite) storage temperatures are estimated using the fsp-liq (Putirka, 2008), cpx-liq and cpx-only thermometers (Jorgenson et al., 2022). To estimate pressure, we applied the cpx-liq barometer of Putirka et al. (1996), Neave and Putirka (2017) and Jorgenson et al. (2022) for the basaltic compositions, and the cpx-liq and cpx-only barometers of Jorgenson et al. (2022) for the comendites and pantellerites respectively. In addition, we applied the QUILF model (Anderson et al., 1993) on the co-existing cpx-opx pairs in peralkaline rocks to retrieve the two-pyroxene equilibrium temperature and pressure conditions. The augites in the pantelleritic rocks have a close to zero (0.72-0.98) enstatite components, and the orthopyroxenes have compositionally distinct cores that are considered antycrystic (section 4.4). This low Fe content and disequilibrium texture of the two components may lead to an error message or high uncertainty (i.e. ±>400°C), as the QUILF93 program may be unable to calculate the corresponding derivatives (Anderson et al., 1993). On the other hand, the two pyroxenes in the comenditic rocks are within analytical uncertainty of the QUILF model and suggest equilibrium conditions. Therefore, we only reported the QUILF model temperature and pressure estimate for the comenditic compositional range. The geothermobarometry results of the BBTM samples are presented in the Supplementary Information (SI-5).

We used the H_2O_{diff} of glass and melt inclusions as the liquid water content for all H_2O-dependent thermobarometers. The relative probability of the pre-eruptive temperature and pressure estimates of all BBTM rock suites are shown as kernel density estimation (KDE) plots on Figures 12 and 13 respectively, with the precision (Standard Error of Estimates, SEE) of each mineral-liquid pair geothermobarometer shown as an error bar.

The basaltic rock temperature estimates from the cpx-liq (1070-1190 °C), fsp-liq (1090-1125 °C) and ol-liq (1145-1160 °C) thermometers are broadly consistent and overlap within the 1070 °C to 1190 °C range (Fig. 12a). The modal temperature peak for the basalts is between 1100 to 1190 °C (Fig. 12a). However, the cpx-liq temperature estimate for the basalts based on Jorgenson et al. (2022) is 60 °C lower than that estimated using the equation of Putirka et al. (1996) and Putirka (2008), and the fsp-liq thermometer displays two modes representing samples from different scoria cones (MER157: 1084-1100 °C; MER234: 1108-1124°C; Fig. 12a). The ol-liq thermometer after Putirka et al. (2007) gave a restricted temperature result (~1150 °C) within the allowed Kd(Fe-Mg) range.

The comendites record two overlapping storage temperature clusters using the cpx-liq, cpx-only, QUILF and fsp-liq thermometers, representing the TM-P2 and TM-P1 deposits. The cpx-liq estimates for comendite based on Jorgenson et al. (2022) yielded 920-940 °C and

915-940 °C for TM-P1 and TM-P2 respectively (Fig. 12b), while the cpx-only thermometer gives 925-1041 °C (TM-P1) and 860-950 °C (TM-P2). The cpx-opx equilibria using the QUILF model estimate a storage temperature of 930-1000°C (TM-P1) and 990-1000 °C (TM-P2). The fsp-liq thermometer after Putirka (2008) estimated a generally lower value and also a narrower range (TM-P1: 820-900 °C; TM-P2: 805-815 °C; Fig. 12b) relative to the cpx-liq, cpx-only and QUILF thermometers.

The cpx-liq and cpx-only thermometer for pantellerite samples gives a consistent estimate of 890-900°C and 860 °C, respectively. The fsp-liq pair captures lower values relative to cpx-liq and cpx-only, and it clusters into two non-overlapping temperature ranges of 700-730 °C and 745-765 °C, representing Baricha and Meki (and isolated pumice cones) deposits respectively (Fig. 12c). The high temperatures of the pantellerites are consistent with the relatively Al_2O_3-rich nature of the alkali feldspars (typically >18.5 wt%) in the Meki and pumice cone deposits (Section 4.4). For all rock suites, there is no significant difference between the rim and core temperature results (Figure 12).

A wide storage pressure range of 0-800 MPa is obtained for all BBTM samples. The basaltic rocks estimates fall within 90-800 MPa using the Putirka et al. (1996), Neave and Putirka (2017) and Jorgenson et al. (2022) barometers. The Putirka et al. (1996) barometer gives relatively higher and wider pressure (190-800 MPa) estimates than those of Neave and Putirka (2017) and Jorgenson et al. (2022). If we consider the highest-probability peaks on the KDE plots, the storage pressure falls in a narrower range between 200-800 MPa. The comendites have two overlapping storage pressure clusters related to the different TM-P2 and TM-P1 units. The Jorgenson et al. (2022) cpx-liq barometer returns 175-210 MPa and 170-275 MPa storage pressures for TM-P1 and TM-P2 respectively, both with well-defined peaks around 200 MPa on the KDE plots (Fig. 13b). The QUILF model gives a consistent storage pressure of ~225 MPa for TM-P1 and TM-P2. The cpx-only barometer after Jorgenson et al.

(2022) estimated generally lower values for TM-P1 (0-175 MPa) and TM-P2 (175-210 MPa) with a well-defined peak at 100 MPa on the KDE plots (Fig. 13b). The cpx-liq barometer for the pantellerite yields a storage pressure of 200 MPa. This storage pressure estimate is higher than the 100 MPa result of the cpx-only barometer. We did not observe any noticeable difference between core and rim pressure estimates for any of the BBTM rocks (Fig. 13).

5. Discussion

5.1. Magma types

The BBTM eruptive products bulk rock and glass compositions span three distinct compositions: basaltic, comenditic and pantelleritic (Table 1). This is consistent with previous literature that focused on a more limited numbers or and types of samples (Bizouard and Di Paola, 1978; Fontijn et al., 2018; Tadesse et al., 2022).

The basaltic lava flows and scoria cones in the highly faulted eastern sector of the volcanic complex are characterised by relatively less evolved whole rock compositions (49.6 ± 2 wt% SiO_2, 40 ± 5 Mg#, 24.5 ± 15 ppm Ni). Their relatively flat HREE pattern (1.3-1.9 Tb_n/Yb_n) and low ratios for some elements (0.6 ± 0.07 CaO/Al_2O_3 and 5.7 ± 0.4 Zr/Y), suggest that the basaltic magmas originate from a garnet-free magma source. In comparison with the average value of primitive MORB (e.g., Ba/Nb: 5.6; Gale et al., 2013), the basaltic magma has lower Mg# (<56), lower compatible element concentrations (e.g. <80 ppm Ni) and relatively higher values of some index elemental ratios (e.g. Ba/Nb: 8.8 ± 3). This may be a consequence of crustal contamination (Ba/Nb=57 in crust; Rudnick and Gao, 2003), differentiation or an enriched mantle source (e.g., Ayalew et al., 2016). Rhyolite-MELTS fractionation modelling using melt inclusions in olivine as an initial composition generates slightly evolved basaltic magma compositions in the MER from deep (at ca. 510 MPa) fractional crystallization (Nicotra et al., 2021). The basaltic magma in BBTM is generated by a higher degree of fractionation (40-50%) relative to basaltic magma located further north in the MER (Nicotra et al., 2021). The mineral phases in the basaltic rocks are characterised by Na-poor feldspars (i.e. An_{56-85}), and subordinate minerals such as Fe-poor clinopyroxene (diopside; Fs_{13-18}) and Fe-Ti oxides (2 ± 0.2 apfu Fe_t).

The second compositional variety of the BBTM rocks is comendite. The rhyolite lava flows, domes, obsidian coulees and minor pyroclastics (e.g. Tullu Moye) in the eastern sector of the volcanic complex belong to this compositional magma type. The comendite magma is highly evolved with elevated whole rock SiO_2 (72 ± 2 wt%) and Zr (646 ± 113 ppm) contents (Table 1). Tadesse et al. (2022) identified that the Tullu Moye edifice experienced at least two different explosive eruptions in the past (i.e. TM-P1 and TM-P2; Tadesse et al., 2022). Whilst their whole rock composition is highly similar, the glass chemical composition of these two eruptions significantly varies, e.g. in Al_2O_3 and FeO contents (Fig. 4), suggesting they are either two distinct comendite magmas or they represent the same magma that has experienced different amount of crystallisation. We refer these two comendite magma compositions as TM-P1 and TM-P2 comendites, representing the older TM-P1 and the younger TM-P2, respectively (Table 1). The TM-P1 comenditic magma has higher Al_2O_3 and lower FeO contents than the TM-P2 comendite. The mineral assemblage of TM-P1 consists mainly of plagioclase feldspars (An_{18-58}), whereas TM-P2 does not contain plagioclase, but only anorthoclase feldspar (Or_{19-27}). On the mineral classification diagram (Fig. 9a) the feldspars from TM-P1 and TM-P2 show a wide range of Na content that may be related by a linear evolution trend. The distinct chemistry of both deposits is also apparent in the other subordinate mineral phases such as clinopyroxene (TM-P1: Fs_{14-23} and TM-P2: Fs_{22-44}) and titanomagnetite (TM-P1: 0.3 ± 0.005 apfu Ti and TM-P2: 0.5 ± 0.01 apfu Ti). The clinopyroxene and titanomagnetite minerals in the more evolved TM-P2 comenditic melt are enriched in Fe and Ti, respectively.

The third bulk compositional variety in the BBTM is pantellerite, which is predominantly found as pyroclastics deposits and lava flows / domes in the western and central sectors of the volcanic complex. The deposits from the caldera-forming eruptions (Suke and Meki), major edifices (Bora, Baricha), pumice cones and rhyolite lava / domes (e.g. Jima) belong to this compositional series. These rocks contain aenigmatite and sanidine in their mineral assemblage, which are not observed in the basaltic or comenditic rocks. The pantelleritic magma is the most evolved magma in the BBTM (SiO_2:73.8 ± 1.5 wt%; Zr: 993 ± 332 ppm). The incompatible trace element concentrations are comparable to some volcanoes in the MER (e.g., Aluto: 915 ± 365 ppm Zr; Gedemsa: 617 ± 449 ppm Zr) and Afar rift (Debbahu: 947 ± 337 ppm Zr; Hutchison et al., 2018 and references therein), but generally lower than those of the Olkaria (Kenya) volcanic complex (e.g., 1312 ± 678 ppm Zr; Marshall et al., 2009) and Pantelleria, Italy (e.g., 1640 ± 476 ppm Zr; White et al., 2009). The glass composition of the pantelleritic rocks shows two sub groups (high-Al and low-Al; Table 1). On average, Baricha pyroclastic deposits (low-Al) are characterised by a slightly lower Al_2O_3 content (8.8-10.6 wt%) relative to the other pantelleritic eruptive products (high-Al; Al_2O_3: 9.8-12.4 wt%). The mineralogical assemblage of the pantellerites consists predominantly of alkali feldspar with minor augite, enstatite, Ca-Na amphibole, aenigmatite and quartz. There is a systematic Al_2O_3 enrichment and Na_2O depletion in the alkali feldspar composition through the stratigraphy (i.e., MER253; Tadesse et al., 2022), consistent with the aenigmatite's Ti depletion. This trend in the glass, feldspar and aenigmatite composition might suggest some temporal evolution of the pantelleritic magma. Overall, the feldspars and clinopyroxenes identified in the pantelleritic magma are enriched in K and Fe respectively, relative to the basaltic and comenditic magmas. The peralkaline magmas in the MER are more volatile-rich, pre-dominantly in H_2O (<2-8 wt%), than the basaltic magmas (2 to <0.5 wt% H_2O; Iddon et al., 2020).

The bulk trace element compositions are important to pin point the source relationships of compositionally distinct magmas (e.g. Hutchison et al., 2016b; Tadesse et al., 2019). The BBTM rocks' REE and spider diagrams show a generally parallel pattern (Fig. 7). Additionally, highly incompatible elements plotted against Zr (Fig. 6) display generally linear trends, and the systematic behaviour of those elements. These trends suggest that basaltic, comenditic and pantelleritic magmas share a single magmatic lineage. The narrow range of highly incompatible element ratios (e.g. Zr/Hf: 36-42) within the BBTM also indicates a source resemblance. A minor deviation of some samples on the trace element plots (Fig. 6-7) may relate to a slight involvement of crustal material. Given that incompatible elements are enriched in the crust, crustal material involvement is evaluated using contamination index La/Nb and the Ta pattern on the spider diagram. A few BBTM samples (n=3) consistently show very low La/Nb ratios (<0.7) and anomalously high Ta positive spikes (Fig. 6-7).

5.2. Magma genesis

Several studies proposed that pantelleritic magmas in the Ethiopian Rift and elsewhere are derived via extreme fractional crystallisation of a basaltic parental magma (e.g. White et al., 2009; Marshall et al., 2009; Giordano et al., 2014; Hutchison et al., 2016b, 2018; Iddon et al., 2019; Tadesse et al., 2019). The BBTM bulk rock and glass data indeed consistently display fractional crystallisation as the most likely governing process driving magmatic differentiation. The small variation in incompatible element ratios (e.g. La/Lu: 70-90) throughout the entire BBTM suite is consistent with fractional crystallisation processes. The negative correlation of MgO, FeO, CaO and TiO_2 against SiO_2 (Fig. 5) in the bulk rock chemistry indicates fractionation of minerals such as olivine, clinopyroxene, Fe-Ti oxides (ulvöspinel-magnetite series) and Ca-rich plagioclase from the basaltic magma at an early stage. This is further supported by negative trends of compatible trace elements (Ni, Co and Sr; Fig. 6). The positive-negative correlation trends of Al_2O_3 and P_2O_5 against the differentiation index indicates the later precipitation of Na-rich plagioclase and apatite respectively, along the liquid line of descent. Moreover, the near-vertical negative correlation of Ba with Zr and Na_2O with SiO_2 in the evolved compositions indicates the role of alkali feldspar crystallisation in the evolution of the residual magma from comenditic to pantelleritic at the final stage. Similarly, the rocks representing the different evolution stages show a variation in mineral assemblages from basalt (olivine + clinopyroxene + Ca-rich plagioclase ± titanomagnetite) through comendite (plagioclase feldspar + titanomagnetite ± clinopyroxene ± orthopyroxene ± amphibole) and finally to pantellerite pyroclastic products (alkali feldspar + aenigmatite ± clinopyroxene ± quartz ± amphibole). The evolution trend is also apparent from the gradual SiO_2 enrichment in the glass, and Fe enrichment (in clinopyroxene and titanomagnetite) and Na depletion (in feldspar) in minerals that are commonly present in all BBTM rocks. However, if we closely examine the trends of highly incompatible elements such as Nb, Hf, Y and La against Zr (Fig. 6 and SI-4), there is a slight shift of the linear trend after 750 ppm Zr. This is the critical point on the liquid line of descent at which the composition changes from a comenditic to a pantelleritic liquid.

Enclaves of different mineralogical composition relative to the host rocks are observed in the deposits at a few locations and may suggest that other processes contribute to magmatic differentiation than fractional crystallisation alone. A xenolith composed of mafic minerals was identified in the Togee lava dome at the centre of the volcanic complex (Fig. 3a). Its basaltic nodules might come from magma-country rock interaction or magma mixing. The bulk rock chemistry of the Togee lava dome has unique Eu and Nb compositions relative to other comendites as a result of plagioclase accumulation and/or crustal assimilation. Stratigraphic sections such as MER251 and MER373 located near Oda and Tullu Moye volcano respectively, preserved interbedded scoria and pumice layers. The composition of the scoria is slightly more evolved (47 wt% SiO_2; 137 ppm Zr) than the basaltic magma. On the other hand, the pumice layers have a less evolved composition (66 wt% SiO_2; 432 ppm Zr) than the comenditic and pantelleritic magmas. All analyses from these outcrops plot between the ranges of the basaltic and comenditic magmas on the TAS diagram (Fig. 4a) suggesting mafic-felsic magma interaction to produce these intermediate compositions. Other centres in the MER, such as Aluto (Hutchison et al. 2016b), Boset-Bericha (Ronga et al. 2010; Macdonald et al. 2012) and Chefe Donsa (Rooney et al. 2012), also record small proportions of intermediate rocks that are interpreted to result from crustal assimilation and/or magma mixing.

Intermediate magma compositions are rarely observed at BBTM (e.g., rare enclaves and eruptive products) relative to the peralkaline magma that is predicted to form from fractionation. This compositional gap is often referred to as the "Daly Gap" (Bunsen, 1851; Daly, 1925) and is also observed at other MER volcanoes (e.g., Aluto: Hutchison et al., 2016b; Gleeson et al., 2018). The trace element and feldspar compositions of BBTM products preserve crystallisation paths with narrow or no compositional jumps. There is however some evidence of intermediate compositions in the melt inclusions trapped within some mineral phases (section 4.3). Together with the gradual trends of the trace element and feldspar compositions, these melt inclusions support the formation of intermediate compositions by the magmatic differentiation processes. A narrow crystallisation interval from 50 to 64 wt% SiO_2 due to extraction of SiO_2-poor phases (e.g. spinel) has been proposed for generating a small amount of intermediate melt (Mushkin et al., 2002; White et al., 2009). The generally low magma viscosity could allow rapid physical separation of the SiO_2-poor minerals via crystal settling in the magma reservoir, which might facilitate the generation of the Daly Gap (Neave et al., 2012). The small amount of intermediate magma generated and its non-eruption, possibly due to mechanical trapping from high melt density and/or high crystal loads (e.g. Peccerillo et al., 2003; Neavi et al., 2012; Gleeson et al., 2018; Tadesse et al., 2019; Iddon et al., 2019), may explain the low proportions of intermediate magmas observed at the surface.

5.3. Pre-eruptive storage conditions

The temperature estimation of the basaltic magma from the fsp-liq thermometer (1090-1125 °C) generally show lower values relative to the cpx-liq (1070-1190 °C) and ol-liq pairs (1145-1160 °C). This variation in the temperature estimation may result from the order of the mineral saturation in the melt or the artefacts of the applied thermometers. Moreover, in this magma most olivine crystals are not in equilibrium with the carrier liquid (Fig. 12a), showing resorbed textures and complex mineral zoning. This relative dominance of antecrysts over phenocrysts is higher in the scoria samples than in the lava, indicating that the olivine antecrysts represent crystals picked up from deeper magma input that likely drive more energetic eruption.

The mineral phases for the thermometer calculations in the comenditic rocks are mostly in equilibrium with the melt as confirmed from physical mineral-melt contact and the Fe-Mg exchange coefficient. The comendite magma temperature estimation suggests two distinct clusters from the fsp-liq thermometer, i.e. 820-900 °C (TM-P1) and 805-815 °C (TM-P2) for the older and younger Tullu Moye deposits respectively. However, the cpx-liq, cpx-only and QUILF thermometers yield overlapping and higher storage temperatures for both Tullu Moye eruptions (890-1000 °C). The >900 °C temperature estimation of the cpx-liq, cpx-only and QUILF thermometers is not consistent with the experimental results on the peralkaline suites (Scaillet and Macdonald, 2003; Di Carlo et al., 2010; Romano et al., 2020). Our test on Jorgenson et al. (2022) cpx-liq and cpx-only thermometers using Scaillet and Macdonald (2003) clinopyroxene and equilibrium liquid shows an elevated temperature estimate (up to ±200 °C) than the experiment isothermal condition. Similarly, the QUILF model likely overestimates the storage temperature since the model does not performs very well on highly evolved, olivine- and ilmenite-free peralkaline compositions (Anderson et al., 1993; Ren et al., 2006). Moreover, the fsp-liq thermometer of Putirka (2008) gives very close temperature estimates to those of the experimental conditions of Scaillet and Macdonald (2003; SI-5). The two different temperature clusters of the comendite magma captured by the fsp-liq thermometers correspond to the compositional clusters in the glass and mineral analyses. There is however no variation in mineral assemblages or whole rock compositions. Therefore the two clusters in the pre-eruptive temperature (as captured by the fsp-liq thermometer), glass chemistry and mineral chemistry suggest an evolution of the comendite magma before eruption. The TM-P1 comendite magma evolved towards lower Al_2O_3 with decreasing temperature (i.e., TM-P2). Mineral phases such as clinopyroxene in TM-P2 indeed show cores richer in Al, Fe and Ti relative to the rims. This suggests that the clinopyroxene crystals capture variable equilibration histories in response to variable magma storage conditions. Estimations from the cpx-liq and fsp-liq thermometers do not capture this core-rim compositional variation, which may indicate small changes in temperature within the model's error of estimation.

The pantelleritic magma is the coldest magma types in the BBTM, as suggested by cpx (i.e., cpx-liq and cpx-only: 860-900 °C) and fsp (i.e., fsp-liq: 730-745 °C) related thermometers. The BBTM pantelleritic rocks are amphibole-and aenigmatite-phyric. Experimental data by Romano et al. (2020) indicate aenigmatite is stable at ≤750 °C (H_2O_{melt}–poor conditions) or ≤680 °C (water-saturated conditions). In addition, we tested the applied thermometers on Romano's et al. (2020) cpx and fsp experimental compositions. This shows that the cpx-liq and cpx-only thermometers of Jorgenson et al. (2022) overestimate by up to 230 °C. On the other hand, the fsp-liq thermometer of Putirka (2008) gives very close temperature estimates to the isothermal conditions of the experiments of Romano et al. (2020), and it also agrees with the temperature stability fields of critical mineral phases (i.e., amphibole, aenigmatite).

Therefore, our BBTM pantelleritic magma cpx-based temperature estimates (860-900 °C) are likely to high, while estimates from the fsp-liq thermometer are likely to be more accurate. The low-Al magma yields a relatively low temperature (700-730 °C) compared to the high-Al pantellerite (745-765 °C) as captured by the fsp-liq thermometers. The BBTM pantellerites' pre-eruptive temperature estimates coincide with the 718-765 ± 23 °C interval estimated for Aluto pantellerites (Gleeson et al., 2017). The temperature variation in the BBTM pantellerites is also consistent with the Al_2O_3 depletion in glass compositions for Baricha relative to the high-Al pantellerites. If we combine this with stratigraphic relationships, the pantelleritic magma within the same suite evolves to Al_2O_3-poor and colder magma moving up in the stratigraphy.

The storage pressure estimations of the BBTM magmatic reservoirs are mainly based on the cpx-liq, cpx-only and QUILF barometers. The basaltic magma has higher and wider pre-eruptive storage pressures (200-800 MPa, high peak in KDE plot; Fig. 13) compared to the peralkaline magmas. The cpx-liq barometer of Neave and Putirka (2017) is designed for tholeiitic basalts; and as a consequence it gives an underestimated storage pressure for basalts with alkaline affinity (e.g., BBTM basalts). In contrast, the Putirka et al. (1996) barometer is calibrated for alkaline basalt and gives more realistic pressure estimates for the BBTM basaltic magma (190-800 MPa). This barometer (i.e., Putrika et al., 1996) is also suitable for anhydrous mafic compositions and is therefore applicable to depleted MER basalts, which likely contains <2 wt% H_2O (Iddon et al., 2020). Similar to the thermometers, the performance of the cpx-only barometer is much better than that of the cpx-liq barometer and QUILF model for the peralkaline magma (SI-5). In contrast to their temperature, the comenditic and pantelleritic magmas show overlapping storage pressures of <210 MPa with a mode at 100 MPa (Fig. 13). The experimental data on peralkaline melts suggests a requirement of ≥100 MPa for aenigmatite stability (Di Carlo et al., 2010), which is consistent with our estimates. The value is also consistent with the ca. 100 MPa estimate from Rhyolite-MELTS modelling on evolved peralkaline melts at other MER volcanoes such as Aluto (Gleeson et al., 2017), Kone and Fentale (Iddon et al., 2019).

The peralkaline magma redox conditions are well constrained by experimental work on comendite (Scaillet and Macdonald, 2003) and pantellerite melts (Di Carlo et al., 2010; Romano et al., 2020). Experimental data suggests that only low fO_2 (below QFM buffer) conditions favour the formation of peralkaline magma.

Magma storage depths are calculated from the estimated pressures by assuming 2,800 kg/m^3 average crustal density in the MER (Wilks et al., 2017), across the entire crust which is ca. 34 km thick under the BBTM region (Dugda et al., 2005). Using this conversion, the basaltic magma is stored at depths of 7-29 ± 5 km (Fig. 14; Table 1). This estimation is similar to the estimated basaltic magma storage depths at Kone (15-21 ± 5 km; Iddon et al., 2019). The peralkaline (comendite and pantellerite) magma is stored at depths of ca. 4 ± 11 km (Fig. 14; Table 1). This latter estimate is broadly consistent with estimates for shallow magmatic storage depths at other silicic MER volcanoes (e.g., Gleeson et al., 2018; Iddone et al., 2019).

Geophysical observations can provide further constraints on magma storage and transportation (e.g. White et al., 2019). Regional gravity surveys have revealed 4-20 km deep intrusions along the MER floor concomitant with the silicic volcanoes (Mehatsente et al., 1999). The recent temporarily deployed seismic network (Greenfield et al., 2019a, b) across BBTM displayed seismicity, which is associated with hydrothermal circulation in two main locations, one centred on Bora-Baricha and another around Tullu Moye. InSAR surveys (Biggs et al., 2011; Albino and Biggs, 2021) further confirm active ground deformation from a shallow source (<2.5 km depth, 3-10 km source radius) in the region between the three main volcanic edifices in the complex (i.e., Bora, Baricha and Tullu Moye). This observation is consistent with our petrogenetic modelling of the shallow pantelleritic and comenditic magmas reservoirs located beneath the west-central (Bora-Baricha) and eastern (Tullu Moye) sectors of the volcanic complex. The magnetotelluric survey by Samrock et al. (2018; 2021) in the Tullu Moye region indeed identified highly conductive zones at ca. 4 km and 14 km depth, interpreted as melt rich zones (12-35% melt) at different depths, and that are interconnected by an electrically conductive conduit-like zone. Their survey results overlap with our estimated depths for the peralkaline (4 ± 11 km) and basaltic (7-29 ± 5 km) magma reservoirs beneath Tullu Moye. The magnetotelluric methods have however not identified any increased electrical conductivity at shallow depth in the central and western portion of the volcanic complex, i.e. in the area where we estimate pantelleritic magma reservoirs to be stored. The electrical conductivity of the magmatic reservoirs is dependent on the nature of the magmas including their volatile content, temperature, composition and crystal content (Gaillard and Marziano, 2005). The non-visibility of pantelleritic melt by the magnetotelluric surveys is also observed elsewhere in the MER and may be related to the presence of high-resistivity crystal-rich (e.g., at Aluto, Samrock et al., 2015, 2021; Hübert et al., 2018) and/or small-volume ephemeral melt lenses below the spatial resolution (<1 km) of the technique (e.g., Fabbro et al., 2017; Cashman et al., 2017). The coherence of the geothermobarometry modelling with geophysical observations suggests consistent magma storage is responsible for the pre-historic eruptions at BBTM.

5.4. Magmatic plumbing system

The BBTM volcanic complex provides a good opportunity to investigate a peralkaline magmatic plumbing system in the MER in an area where both basaltic and rhyolitic magmas are erupted. A trans-crustal magmatic architecture in the BBTM was previously proposed by Samrock et al. (2018) based on magnetotelluric data. Nazzareni’s et al. (2020) clinopyroxene barometry overview of MER rocks (including BBTM) suggests a continuous range of crystallisation pressures starting from the crust-mantle boundary (i.e., 1000 MPa = 35 km) up to the main storage depths at about 15-20 km (Fig. 14b). At this depth, the magmatic reservoirs are most likely to be in the form of vertically stacked sills, controlled by the regional stress field (Maccaferri et al., 2014). At these depths the magma starts to crystallise olivine, clinopyroxene and orthopyroxene, modifying the primitive magma composition (Nazzareni et al., 2020; Nicotra et al., 2021). At this point the magma is ~1130 °C hot and eruptible, and could reach the Earth's surface following major structural pathways defined by the extensional stress regime (e.g., Mazzarani et al., 2016). At BBTM, these eruptions are represented by basaltic fissures and small eruptive centres in the heavily faulted eastern sector (Fig. 1). If not erupted, the basaltic magmas may become buoyant and follow a feeding channel to shallower reservoirs constrained by the regional stress field, as suggested from the magnetotelluric 3D phase tensor inversion model of Samrock et al. (2018).

The shallower magma storage zone (i.e., ~5-10 km) is characterised by peralkaline melt that results from fractionation and minor assimilation. In some cases the less evolved basaltic magma forms ephemeral melt lenses at shallow depth before eruption. At these depths the stress field favours the formation of horizontally stacked sills (Maccaferri et al., 2014). The storage reservoirs are horizontally very limited by the recent faults and appear like pocket lenses (e.g., Samrock et al., 2018; Iddon et al., 2019). However, in Afar peralkaline magmas are stored at similar depths, and thought to form laterally extensive and well-connected reservoirs (Pagli et al., 2012; Field et al., 2012; Desissa et al., 2013). The eastern sector of the BBTM volcanic complex is highly affected by faults (Agostini et al., 2011), and channels out the comendite melts at the earlier-intermediate stages of differentiation. The western and central sectors of the volcanic complex are less affected by the recent faults and are instead predominantly affected by surface loading stresses that result from the presence of volcanic edifices or caldera infill (Xu et al., 2017 and references therein). This allows the peralkaline melt to reside at shallow crustal levels for longer times and evolve to pantelleritic compositions, characteristic for most silicic MER complexes (e.g., Peccerillo et al., 2003; Gleeson et al., 2017; Iddon et al., 2018).

6. Conclusion

We present the petrological and geochemical characteristics of the magmas responsible for the generation of lava and pyroclastic volcanic products in the BBTM volcanic complex. The data set includes petrography, bulk major and trace element composition and major element compositions of phenocryst phases, groundmass and melt inclusions. The bulk rock compositions vary from basalt to peralkaline rhyolite (comendite and pantellerite), and the chemical variability can be largely explained by fractional crystallisation processes with minor crustal assimilation and magma mixing. The mineral assemblages in the different rock compositions vary from plagioclase feldspar (An_{56-85}) + olivine (Fo_{50-84}) + diopside (Wo_{37-47}, En_{35-45}, Fs_{13-18}) + titanomagnetite in the basalts, and plagioclase feldspar (An_{18-58}) + alkali feldspars (Or_{2-78}) + aenigmatite + augite/hedenbergite (Wo_{39-44}, En_{15-44}, Fs_{14-44}) ± titanomagnetite ± quartz ± amphibole in the peralkaline rhyolites, which evolve along the liquid line of descent. The dominant mineral phases such as clinopyroxene and feldspars show a tendency for Fe and Na enrichment, respectively as they evolve from basaltic to pantelleritic compositions. The comendite and pantellerite deposits show systematic variations towards more evolved glass and mineral compositions through the stratigraphy.

The combination of thermometry (i.e., clinopyroxene-liquid, feldspar-liquid, olivine-liquid and clinopyroxene-only) and barometry (i.e., clinopyroxene-liquid and clinopyroxene-only) suggests that the basaltic magmas are stored at high temperature (1070-1190 °C) at mid- to deep-crustal levels (~7-29 km). The peralkaline melts are stored at lower temperatures (i.e., 805-900 °C for comendite and 700-765 °C for pantellerite) at shallow crustal levels (~4 km). The conditions of pre-eruptive storage as recorded in the comendite and pantellerite rocks in combination with stratigraphic constraints, suggest the temporal evolution of the magma reservoirs to cooler storage temperatures. The correlation of the petrological modelling and geophysical observations suggest similar magma storage conditions could be responsible for past small and large-scale eruptions and the current hydrothermal circulation that induces low-frequency seismicity, ground deformation and geothermal activity in the volcanic complex.

Acknowledgements

AT is supported by a Fonds National de la Recherche Scientifique (F.R.S.-FNRS) Aspirant doctoral scholarship. Several samples and an extensive mineral chemistry dataset were collected under the NERC-funded RiftVolc Large Grant (NE/L013649/1) by KF along with others. KF further acknowledges FNRS MIS grant F.4515.20, and the Wiener Anspach Foundation grant “The Magmatic Evolution of Geothermally Active Calderas in Ethiopia”. VD thanks the F.R.S.-FNRS for support. We would like to thank Tamsin Mather and David Pyle for continued support and giving the permission to access the dataset and samples from the RiftVolc project, which also supported additional fieldwork and laboratory analyses from AT’s PhD work. We sincerely thank Kathy Whaler and Anne Galbraith (University of Edinburgh) for the continued facilitation of the work. Field work and sample export was kindly permitted by authorities of the Oromia region and Ministry of Mines and Petroleum of Ethiopia, respectively. Professional logistical support was provided by Ethioder Pvt Ltd Co and their drivers. Sabrina Cauchies and Cécilia Teller helped with whole rock data collection at ULB. We thank Paul Wallace and Oliver Higgins for the fruitful discussion on geothermobarometry modelling. Our gratitude goes to Gareth Fabbro and John White for detailed and constructive comments which improved the paper. We thank Di-Cheng Zhu for the editorial handling.

Reference

Abebe, B., Boccaletti, M., Mazzuoli, R., Bonini, M., Tortorici, L., Trua, T., 1998. Geological map of the Lake Ziway – Asella region (Main Ethiopian Rift). Scale 1:50,000.

Agostini, A., Bonini, M., Corti, G., Sani, F., Mazzarini, F., 2011. Fault architecture in the Main Ethiopian Rift and comparison with experimental models: implications for rift evolution and Nubia–Somalia kinematics. Earth and Planetary Science Letters, 301(3-4), 479-492.

Albino, F., Biggs, J., 2021. Magmatic Processes in the East African Rift System: Insights From a 2015–2020 Sentinel-1 InSAR Survey. Geochemistry, Geophysics, Geosystems, 22(3), e2020GC009488.

Andersen, D.J., Lindsley, D.H. and Davidson, P.M., 1993. QUILF: A pascal program to assess equilibria among Fe ▪ Mg ▪ Mn ▪ Ti oxides, pyroxenes, olivine, and quartz. Computers & Geosciences, 19(9), pp.1333-1350.

Ayalew, D., Jung, S., Romer, R.L., Kersten, F., Pfänder, J.A. and Garbe-Schönberg, D., 2016. Petrogenesis and origin of modern Ethiopian rift basalts: Constraints from isotope and trace element geochemistry. Lithos, 258, pp.1-14.

Biggs, J., Bastow, I. D., Keir, D., Lewi, E., 2011. Pulses of deformation reveal frequently recurring shallow magmatic activity beneath the Main Ethiopian Rift. Geochemistry, Geophysics, Geosystems, 12(9).

Bizouard, H., Di Paola, G. M., 1978. Mineralogy of the Tullu Moje active volcanic area (Arussi: Ethiopian Rift valley). In Petrology and Geochemistry of Continental Rifts (pp. 87-100). Springer, Dordrecht.

Blundy, J., Cashman, K., 2008. Petrologic reconstruction of magmatic system variables and processes. Reviews in Mineralogy and Geochemistry, 69(1), 179-239.

Boccaletti, M., Bonini, M., Mazzuoli, R., Abebe, B., Piccardi, L., Tortorici, L., 1998. Quaternary oblique extensional tectonics in the Ethiopian Rift (Horn of Africa). Tectonophysics, 287(1-4), 97-116.

Boynton, W. V., 1984. Cosmochemistry of the rare earth elements: meteorite studies. In Developments in geochemistry (Vol. 2, pp. 63-114). Elsevier.

Bunsen, R., 1851. About the processes of volcanic rock formation in Iceland. Annals of Physics , 159 (6), 197-272.

Cashman, K. V., Sparks, R. S. J., Blundy, J. D., 2017. Vertically extensive and unstable magmatic systems: a unified view of igneous processes. Science, 355(6331).

Cassidy, M., Ebmeier, S. K., Helo, C., Watt, S. F. L., Caudron, C., Odell, A., Spaans, K., Kristiano, P., Triastuty, H., Gunawan, H., Castro, J.M., 2019. Explosive eruptions with little warning: Experimental petrology and volcano monitoring observations from the 2014 eruption of Kelud, Indonesia. Geochemistry, Geophysics, Geosystems, 20(8), 4218-4247.

Colby, D. J., Pyle, D. M., Fontijn, K., Mather, T. A., Melaku, A. A., Mengesha, M. A., Yirgu, G., 2022. Stratigraphy and eruptive history of Corbetti Caldera in the Main Ethiopian Rift. Journal of Volcanology and Geothermal Research, 107580.

Corti, G., 2009. Continental rift evolution: from rift initiation to incipient break-up in the Main Ethiopian Rift, East Africa. Earth-Science Reviews, 96(1-2), 1-53.

Daly, R. A., 1925. The geology of Ascension island. In Proceedings of the American Academy of Arts and Sciences (Vol. 60, No. 1, pp. 3-80). American Academy of Arts & Sciences.

Darge, Y. M., Hailu, B. T., Muluneh, A. A., Kidane, T., 2019. Detection of geothermal anomalies using Landsat 8 TIRS data in Tullu Moye geothermal prospect, Main

Ethiopian Rift. International Journal of Applied Earth Observation and Geoinformation, 74, 16-26.

Desissa, M., Johnson, N. E., Whaler, K. A., Hautot, S., Fisseha, S., Dawes, G. J. K., 2013. A mantle magma reservoir beneath an incipient mid-ocean ridge in Afar, Ethiopia. Nature geoscience, 6(10), 861-865.

Di Carlo, I., Rotolo, S. G., Scaillet, B., Buccheri, V., Pichavant, M., 2010. Phase equilibrium constraints on pre-eruptive conditions of recent felsic explosive volcanism at Pantelleria Island, Italy. Journal of Petrology, 51(11), 2245-2276.

Di Paola, G. M., 1972. The Ethiopian Rift Valley (between 7 00′ and 8 40′ lat. north). Bulletin Volcanologique, 36(4), 517-560.

Droop, G. T. R., 1987. A general equation for estimating Fe 3+ concentrations in ferromagnesian silicates and oxides from microprobe analyses, using stoichiometric criteria. Mineralogical magazine, 51(361), 431-435.

Dugda, M. T., Nyblade, A. A., Julia, J., Langston, C. A., Ammon, C. J., Simiyu, S., 2005. Crustal structure in Ethiopia and Kenya from receiver function analysis: Implications for rift development in eastern Africa. Journal of Geophysical Research: Solid Earth, 110(B1).

Ebinger, C., 2005. Continental break-up: the East African perspective. Astronomy & Geophysics, 46(2), 2-16.

Ebinger, C. J., Casey, M., 2001. Continental breakup in magmatic provinces: An Ethiopian example. Geology, 29(6), 527-530.

Edmonds, M., Cashman, K. V., Holness, M., Jackson, M., 2019. Architecture and dynamics of magma reservoirs.

Fabbro, G.N., Druitt, T.H. and Costa, F., 2017. Storage and eruption of silicic magma across the transition from dominantly effusive to caldera-forming states at an arc volcano (Santorini, Greece). Journal of Petrology, 58(12), pp.2429-2464.

Field, L., Blundy, J., Brooker, R. A., Wright, T., Yirgu, G., 2012. Magma storage conditions beneath Dabbahu Volcano (Ethiopia) constrained by petrology, seismicity and satellite geodesy. Bulletin of Volcanology, 74(5), 981-1004.

Fontijn, K., Elburg, M. A., Nikogosian, I. K., Van Bergen, M. J., Ernst, G. G., 2013. Petrology and geochemistry of Late Holocene felsic magmas from Rungwe volcano (Tanzania), with implications for trachytic Rungwe Pumice eruption dynamics. Lithos, 177, 34-53.

Fontijn, K., McNamara, K., Tadesse, A. Z., Pyle, D. M., Dessalegn, F., Hutchison, W., Mather, T.A., Yirgu, G., 2018. Contrasting styles of post-caldera volcanism along the Main Ethiopian Rift: Implications for contemporary volcanic hazards. Journal of Volcanology and Geothermal Research, 356, 90-113.

Fowler, S. J., Spera, F. J., 2010. A metamodel for crustal magmatism: phase equilibria of giant ignimbrites. Journal of Petrology, 51(9), 1783-1830.

Friðleifsson, G. Ó., Ármannsson, H., Guðmundsson, Á., Árnason, K., Mortensen, A. K., Pálsson, B., Einarsson, 2014. Site selection for the well IDDP-1 at Krafla. Geothermics, 49, 9-15.

Gale, A., Dalton, C. A., Langmuir, C. H., Su, Y., Schilling, J. G., 2013. The mean composition of ocean ridge basalts. Geochemistry, Geophysics, Geosystems, 14(3), 489-518.

Gaillard, F., Marziano, G. I., 2005. Electrical conductivity of magma in the course of crystallization controlled by their residual liquid composition. Journal of Geophysical Research: Solid Earth, 110(B6).

Giordano, F., D'Antonio, M., Civetta, L., Tonarini, S., Orsi, G., Ayalew, D., Yirgu, G., Dell'Erba, F., Di Vito, M.A., Isaia, R, 2014. Genesis and evolution of mafic and felsic magmas at Quaternary volcanoes within the Main Ethiopian Rift: Insights from Gedemsa and Fanta'Ale complexes. Lithos, 188, 130-144.

Gleeson, M. L., Stock, M. J., Pyle, D. M., Mather, T. A., Hutchison, W., Yirgu, G., Wade, J., 2017. Constraining magma storage conditions at a restless volcano in the Main Ethiopian Rift using phase equilibria models. Journal of Volcanology and Geothermal Research, 337, 44-61.

Gualda, G. A., Ghiorso, M. S., Lemons, R. V., Carley, T. L., 2012. Rhyolite-MELTS: a modified calibration of MELTS optimized for silica-rich, fluid-bearing magmatic systems. Journal of Petrology, 53(5), 875-890.

Greenfield, T., Keir, D., Kendall, J. M., Ayele, A., 2019a. Low-frequency earthquakes beneath Tullu Moye volcano, Ethiopia, reveal fluid pulses from shallow magma chamber. Earth and Planetary Science Letters, 526, 115782.

Greenfield, T., Keir, D., Kendall, J. M., Ayele, A., 2019b. Seismicity of the Bora-Tullu Moye Volcanic Field, 2016–2017. Geochemistry, Geophysics, Geosystems, 20(2): 548-570.

Hawthorne, F. C., Oberti, R., Harlow, G. E., Maresch, W. V., Martin, R. F., Schumacher, J. C., Welch, M.D., 2012. Nomenclature of the amphibole supergroup. American Mineralogist, 97(11-12), 2031-2048.

Hofmann, A. W., Jochum, K. P., Seufert, M. and White, W. M., 1986. Nb and Pb in oceanic basalts: new constraints on mantle evolution. Earth and Planetary science letters, 79(1-2), 33-45.

Hübert, J., Whaler, K., Fisseha, S., 2018. The electrical structure of the central main Ethiopian Rift as imaged by magnetotellurics: implications for magma storage and pathways. Journal of Geophysical Research: Solid Earth, 123(7), 6019-6032.

Hughes, E. C., Buse, B., Kearns, S. L., Blundy, J. D., Kilgour, G., Mader, H. M., 2019. Low analytical totals in EPMA of hydrous silicate glass due to sub-surface charging: Obtaining accurate volatiles by difference. Chemical Geology, 505, 48-56.

Hutchison, W., Biggs, J., Mather, T. A., Pyle, D. M., Lewi, E., Yirgu, G., Caliro, S., Chiodini, G., Clor, L.E., Fischer, T.P., 2016a. Causes of unrest at silicic calderas in the East African Rift: New constraints from InSAR and soil-gas chemistry at Aluto volcano, Ethiopia. Geochemistry, Geophysics, Geosystems, 17(8), 3008-3030.

Hutchison, W., Pyle, D. M., Mather, T. A., Yirgu, G., Biggs, J., Cohen, B., Barford, D.N., Lewi, E., 2016b. The eruptive history and magmatic evolution of Aluto volcano: new insights into silicic peralkaline volcanism in the Ethiopian rift. Journal of Volcanology and Geothermal Research, 328, 9-33.

Hutchison, W., Mather, T. A., Pyle, D. M., Boyce, A. J., Gleeson, M. L., Yirgu, G., Blundy, J.D., Ferguson, D.J., Vye-Brown, C., Millar, I.L., Sims, K.W., 2018. The evolution of magma during continental rifting: New constraints from the isotopic and trace element signatures of silicic magmas from Ethiopian volcanoes. Earth and Planetary Science Letters, 489, 203-218.

Iddon, F., Jackson, C., Hutchison, W., Fontijn, K., Pyle, D. M., Mather, T. A., Yirgu, G., Edmonds, M., 2019. Mixing and crystal scavenging in the Main Ethiopian Rift revealed by trace element systematics in feldspars and glasses. Geochemistry, Geophysics, Geosystems, 20(1), 230-259.

Iddon, F., Edmonds, M., 2020. Volatile-rich magmas distributed through the upper crust in the Main Ethiopian Rift. Geochemistry, Geophysics, Geosystems, 21(6), e2019GC008904.

Irvine, T. N., Baragar, W. R. A., 1971. A guide to the chemical classification of the common volcanic rocks. Canadian journal of earth sciences, 8(5), 523-548.

Jochum, K. P., Stoll, B., Herwig, K., Willbold, M., Hofmann, A. W., Amini, M., Aurburg, S., Abouchami, W., Hellebrand E. and Raczek, I., 2006. MPI-DING reference glasses for in situ microanalysis: New reference values for element concentrations and isotope ratios. Geochemistry, Geophysics, Geosystems, 7(2).

Jorgenson, C., Higgins, O., Petrelli, M., Bégué, F., Caricchi, L. (2022). A Machine Learning-Based Approach to Clinopyroxene Thermobarometry: Model Optimization and Distribution for Use in Earth Sciences. Journal of Geophysical Research: Solid Earth, 127(4), e2021JB022904.

Keir, D., Bastow, I. D., Corti, G., Mazzarini, F., Rooney, T. O., 2015. The origin of along-rift variations in faulting and magmatism in the Ethiopian Rift. Tectonics, 34(3), 464-477.

Korme, T., 1999. Lithologic and structural mapping of the northeast Lake Ziway area, Ethiopian Rift, with the help of landsat tm data. SINET: Ethiopian Journal of Science, 22(2), 151-174.

Le BAS, M. J., LeMaitre, R. W., Streckeisen, A., Zanettin, B., 1986. Chemical classification of volcanic rocks based on the total alkali-silica diagram. Journal of petrology, 27, 745-750.

Maccaferri, F., Rivalta, E., Keir, D., Acocella, V., 2014. Off-rift volcanism in rift zones determined by crustal unloading. Nature Geoscience, 7(4), 297-300.

Macdonald, R., 1974. Nomenclature and petrochemistry of the peralkaline oversaturated extrusive rocks. Bulletin volcanologique, 38(2), 498-516.

Macdonald, R., Bagiński, B., Ronga, F., Dzierżanowski, P., Lustrino, M., Marzoli, A., Melluso, L., 2012. Evidence for extreme fractionation of peralkaline silicic magmas, the Boseti volcanic complex, Main Ethiopian Rift. Mineralogy and Petrology, 104(3), 163-175.

Mahatsente, R., Jentzsch, G., Jahr, T., 1999. Crustal structure of the Main Ethiopian Rift from gravity data: 3-dimensional modeling. Tectonophysics, 313(4), 363-382.

Marshall, A., Macdonald, R., Rogers, N. W., Fitton, J. G., Tindle, A. G., Nejbert, K., Hinton, R. W., 2009. Fractionation of peralkaline silicic magmas: The greater olkaria volcanic complex, Kenya Rift Valley. Journal of Petrology, 50(2), 323-359.

Martin-Jones, C. M., Lane, C. S., Pearce, N. J., Smith, V. C., Lamb, H. F., Schaebitz, F., Viehberg, F., Brwon, M.C., Frank, U., Asrat, A., 2017. Recurrent explosive eruptions from a high-risk Main Ethiopian Rift volcano throughout the Holocene. Geology, 45(12), 1127-1130.

Mazzarini, F., Le Corvec, N., Isola, I., Favalli, M., 2016. Volcanic field elongation, vent distribution, and tectonic evolution of a continental rift: The Main Ethiopian Rift example. Geosphere, 12(3), 706-720.

McDonough, W. F., Sun, S. S., 1995. The composition of the Earth. Chemical geology, 120(3-4), 223-253.

McNamara, K., Cashman, K. V., Rust, A. C., Fontijn, K., Chalié, F., Tomlinson, E. L., Yirgu, G., 2018. Using lake sediment cores to improve records of volcanism at Aluto volcano in the Main Ethiopian Rift. Geochemistry, Geophysics, Geosystems, 19(9), 3164-3188.

Morimoto, N., Fabries, J., Ferguson, A.K., Ginzburg, I.V., Ross, M., Seifert, F.A., Zussman, J., 1988. Nomenclature of pyroxenes. Mineralogical Journal, 73, 1123-1133.

Mushkin, A., Stein, M., Halicz, L., Navon, O., 2002. The Daly gap: Low-pressure fractionation and heat-loss from cooling magma chamber. Geochimica et Cosmochimica Acta, 66(S1), A539-A539.

Neave, D.A., Fabbro, G., Herd, R.A., Petrone, C.M. and Edmonds, M., 2012. Melting, differentiation and degassing at the Pantelleria volcano, Italy. Journal of Petrology, 53(3), pp.637-663.

Neave, D. A., Putirka, K. D., 2017. A new clinopyroxene-liquid barometer, and implications for magma storage pressures under Icelandic rift zones. American Mineralogist, 102(4), 777-794.

Nazzareni, S., Rossi, S., Petrelli, M., Caricchi, L., 2020. Architecture of the magmatic system in the Main Ethiopian Rift. Dynamic Magma Evolution, 133-151.

Nicotra, E., Viccaro, M., Donato, P., Acocella, V., De Rosa, R., 2021. Catching the Main Ethiopian Rift evolving towards plate divergence. Scientific Reports, 11(1), 1-16.

Pagli, C., Wright, T. J., Ebinger, C. J., Yun, S. H., Cann, J. R., Barnie, T., Ayele, A., 2012. Shallow axial magma chamber at the slow-spreading Erta Ale Ridge. Nature Geoscience, 5(4), 284-288.

Peccerillo, A., Barberio, M. R., Yirgu, G., Ayalew, D., Barbieri, M., Wu, T. W., 2003. Relationships between mafic and peralkaline silicic magmatism in continental rift settings: a petrological, geochemical and isotopic study of the Gedemsa volcano, central Ethiopian rift. Journal of Petrology, 44(11), 2003-2032.

Putirka, K., Johnson, M., Kinzler, R., Longhi, J. and Walker, D., 1996. Thermobarometry of mafic igneous rocks based on clinopyroxene-liquid equilibria, 0–30 kbar. Contributions to Mineralogy and Petrology, 123(1), pp.92-108.

Putirka, K. D., Perfit, M., Ryerson, F. J., Jackson, M. G., 2007. Ambient and excess mantle temperatures, olivine thermometry, and active vs. passive upwelling. Chemical Geology, 241(3-4), 177-206.

Putirka, K. D., 2008. Thermometers and barometers for volcanic systems. Reviews in mineralogy and geochemistry, 69(1), 61-120.

Ren, M., Omenda, P.A., Anthony, E.Y., White, J.C., Macdonald, R. and Bailey, D.K., 2006. Application of the QUILF thermobarometer to the peralkaline trachytes and pantellerites of the Eburru volcanic complex, East African Rift, Kenya. Lithos, 91(1-4), pp.109-124.

Romano, P., Scaillet, B., White, J.C., Andújar, J., Di Carlo, I. and Rotolo, S.G., 2020. Experimental and thermodynamic constraints on mineral equilibrium inpantelleritic magmas. Lithos, 376, p.105793.

Ronga, F., Lustrino, M., Marzoli, A., Melluso, L., 2010. Petrogenesis of a basalt-comendite-pantellerite rock suite: the Boseti Volcanic Complex (Main Ethiopian Rift). Mineralogy and Petrology, 98(1-4), 227-243.

Rooney, T. O., Hart, W. K., Hall, C. M., Ayalew, D., Ghiorso, M. S., Hidalgo, P., Yirgu, G., 2012. Peralkaline magma evolution and the tephra record in the Ethiopian Rift. Contributions to Mineralogy and Petrology, 164(3), 407-426.

Rudnick, R. L., Gao, S., Holland, H. D., Turekian, K. K., 2003. Composition of the continental crust. The crust, 3, 1-64.

Samrock, F., Kuvshinov, A., Bakker, J., Jackson, A., Fisseha, S., 2015. 3-D analysis and interpretation of magnetotelluric data from the Aluto-Langano geothermal field, Ethiopia. Geophysical Journal International, 202(3), 1923-1948.

Samrock, F., Grayver, A. V., Eysteinsson, H., Saar, M. O., 2018. Magnetotelluric image of transcrustal magmatic system beneath the Tullu Moye geothermal prospect in the Ethiopian Rift. Geophysical Research Letters, 45(23), 12-847.

Samrock, F., Grayver, A. V., Bachmann, O., Karakas, Ö., Saar, M. O., 2021. Integrated magnetotelluric and petrological analysis of felsic magma reservoirs: Insights from Ethiopian rift volcanoes. Earth and Planetary Science Letters, 559, 116765.

Saria, E., Calais, E., Stamps, D. S., Delvaux, D., Hartnady, C. J. H., 2014. Present-day kinematics of the East African Rift. Journal of Geophysical Research: Solid Earth, 119(4), 3584-3600.

Stamps, D. S., Saria, E., Kreemer, C., 2018. A geodetic strain rate model for the East African Rift System. Scientific reports, 8(1), 1-9.

Tadesse, A. Z., Ayalew, D., Pik, R., Yirgu, G., Fontijn, K., 2019. Magmatic evolution of the Boku volcanic complex, Main Ethiopian Rift. Journal of African Earth Sciences, 149, 109-130.

Tadesse, A.Z., Fontijn, K., Melaku, A.A., Gebru, E.F., Smith, V.C., Tomlinson, E., Barford, D., Gopon, P., Bégué, F., Caricchi, L., Laha, P., Yirgu, G., Ayalew, D., 2022. Eruption frequency and magnitude in a geothermally active continental rift: The Bora-Baricha-Tullu Moye volcanic complex, Main Ethiopian Rift. Journal of Volcanology and Geothermal Research, 423, 107471.

Trua, T., Deniel, C., Mazzuoli, R., 1999. Crustal control in the genesis of Plio-Quaternary bimodal magmatism of the Main Ethiopian Rift (MER): geochemical and isotopic (Sr, Nd, Pb) evidence. Chemical Geology, 155(3-4), 201-231.

Vidal, C.M., Fontijn, K., Lane, C.S., Asrat, A., Barfod, D., Tomlinson, E.L., Piermattei, A., Hutchison, W., Tadesse, A.Z., Yirgu, G., Deino, A., Moussalam, Y., Mohr, P., Williams, F., Mather, T.A., Pyle, D.M., Oppenheimer, C., 2022. Geochronology and glass geochemistry of major Pleistocene eruptions in the Main Ethiopian Rift: towards a regional tephrostratigraphy. Quaternary Science Reviews, accepted.

Wilks, M., Kendall, J. M., Nowacki, A., Biggs, J., Wookey, J., Birhanu, Y., Ayele, A., Bedada, T., 2017. Seismicity associated with magmatism, faulting and hydrothermal circulation at Aluto Volcano, Main Ethiopian Rift. Journal of Volcanology and Geothermal Research, 340, 52-67.

White, J. C., Parker, D. F., Ren, M., 2009. The origin of trachyte and pantellerite from Pantelleria, Italy: insights from major element, trace element, and thermodynamic modelling. Journal of Volcanology and Geothermal Research, 179(1-2), 33-55.

White, R. S., Edmonds, M., Maclennan, J., Greenfield, T., Agustsdottir, T., 2019. Melt movement through the Icelandic crust. Philosophical Transactions of the Royal Society A, 377(2139), 20180010.

WoldeGabriel, G., Aronson, J. L., Walter, R. C., 1990. Geology, geochronology, and rift basin development in the central sector of the Main Ethiopia Rift. Geological Society of America Bulletin, 102(4), 439-458.

Xu, W., Rivalta, E., Li, X., 2017. Magmatic architecture within a rift segment: Articulate axial magma storage at Erta Ale volcano, Ethiopia. Earth and Planetary Science Letters, 476, 79-86.

Figures

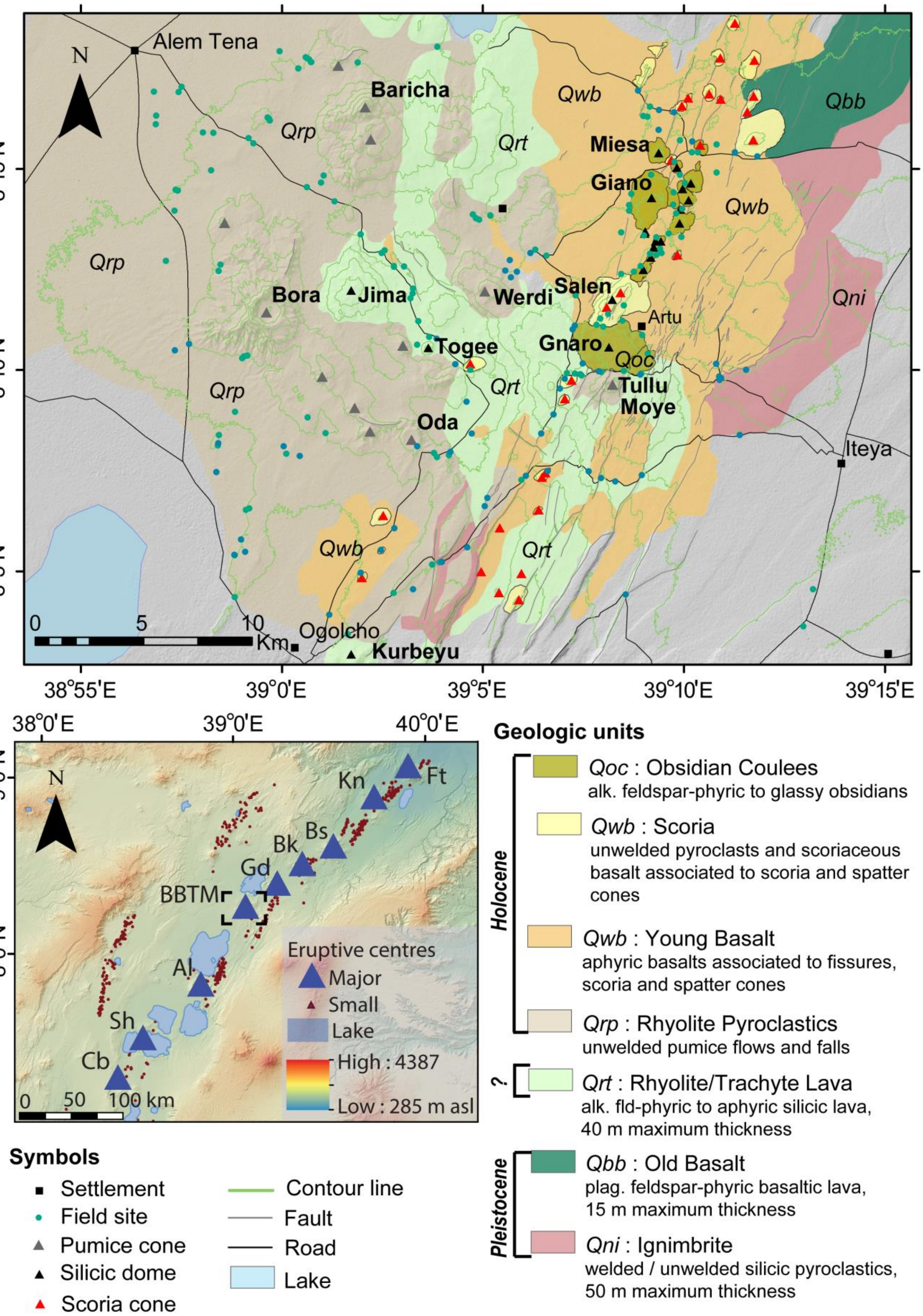

Figure 1: Geological map of BBTM, modified after Abebe et al. (1998), based on constraints from new field observations, petrography and geochemistry (this study). The geological units

are Ignimbrite (Qni), Old basalt (Qbb), Rhyolite / trachyte lava (Qrt), Rhyolite pyroclastics (Qrp), Young basalt (Qwb) and Obsidian coulees (Qoc). The location of BBTM is indicated by a dashed rectangle on the hillshade DEM map processed from Satellite Radar Topography Mission (SRTM) data, showing the distribution of major and small eruptive centres in the MER. The main silicic centres along the rift axis with evidence for significant Late Quaternary activity are indicated by blue triangles, and include Corbetti (Cb), Shala (Sh), Aluto (Al), Bora-Baricha-Tullu Moye (BBTM), Gedemsa (Gd), Boku (Bk), Boset (Bs), Kone (Kn) and Fentale (Fn). The age of the geological units presented on the legend is from WoldeGabriel et al. (1990), Boccaletti et al. (1998) and Tadesse et al. (2022).

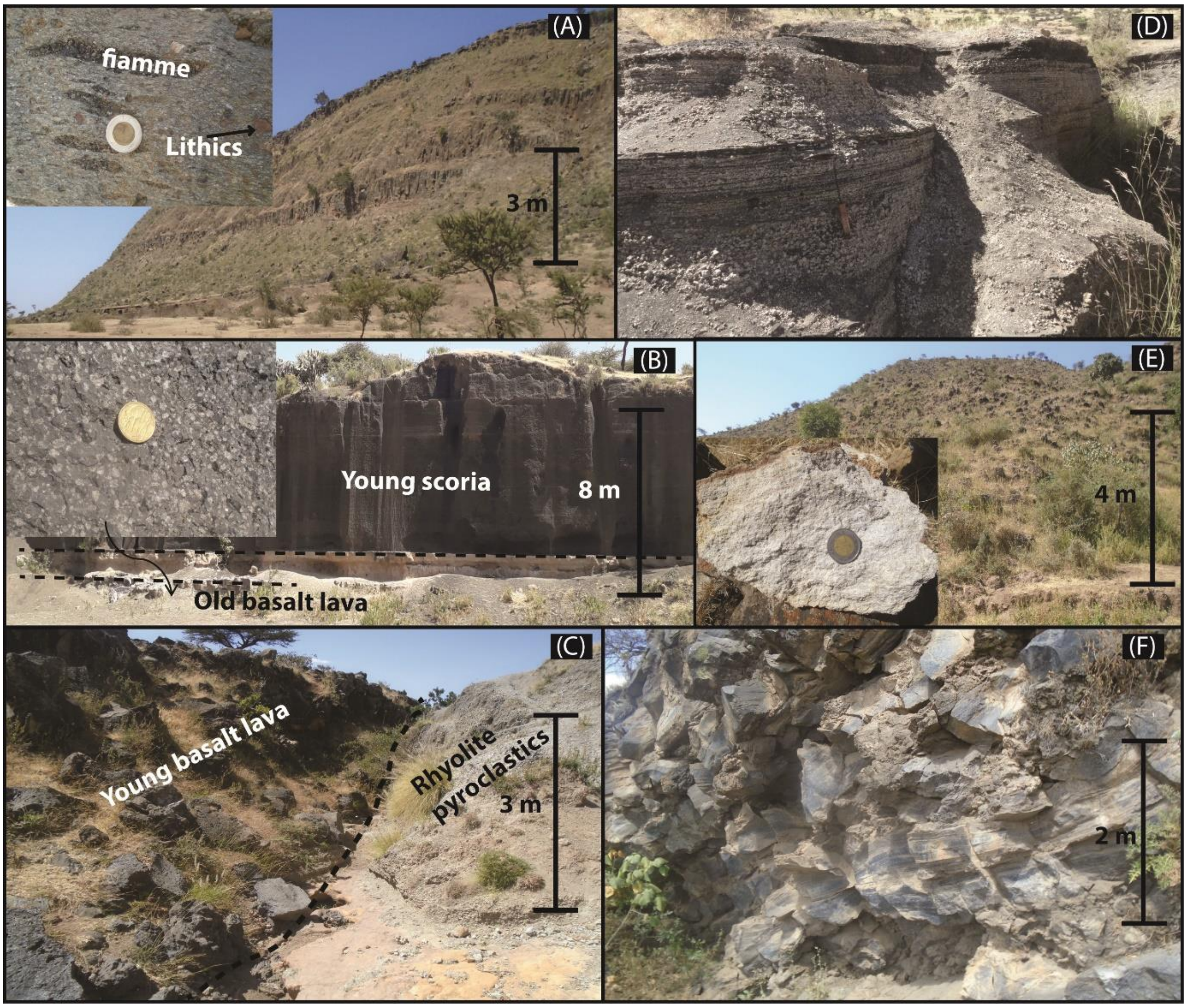

Figure 2: Representative field photos of BBTM eruptive products. (A) Ignimbrite (Qni) exposed along NE-SW fault. (B) Quarry exposure of Old basalt (Qbb) and Young scoria (Qwb) separated by highly altered (lighter) horizon. Note the porphyritic texture of the old basalt on the close-up photo. (C) Young basaltic lava flow (Qwb) blocked by older Werdi rhyolite pyroclastics (Qrp). (D) Interbedded scoria and pumice at section MER251 (Qwb), with alternating proportions along the stratigraphy. (E) Rhyolite lava (Qrt) from the Togee edifice. (F) Obsidian coulees (Qoc) showing flow bands composed of brecciated and vesicular layers.

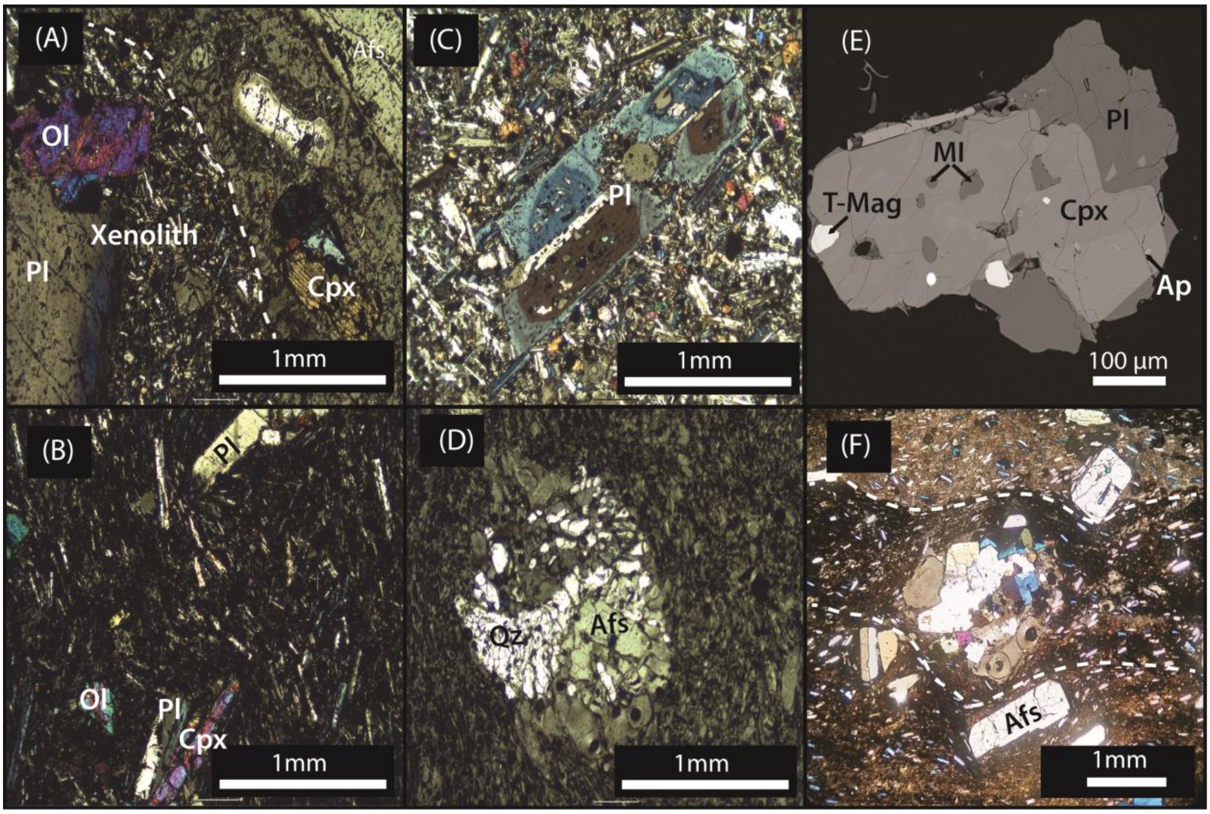

Figure 3: Representative photomicrographs of the BBTM eruptive products. (A) Rhyolite lava from Togee hosting a xenolith (left side of the photo; edge indicated by dashed line). The xenolith is made of olivine (Ol) and plagioclase feldspar (Pl) macrocrysts in a microcrystalline groundmass, whereas the host rock is characterised by alkali feldspar (Afs) and clinopyroxene (Cpx) in a glassy matrix. (B) Young Basalt lava showing microcrystalline texture with identifiable phenocrysts of plagioclase feldspar (Pl), olivine (Ol) and clinopyroxene (Cpx). (C) Old Basalt with holocrystalline texture, showing resorbed and zoned plagioclase feldspar (Pl). (D) Rhyolite Pyroclastics sample from Baricha volcano with glomerocryst clots of alkali feldspar (Afs) and quartz (Qz) intergrowths in a glassy groundmass. (E) Clinopyroxene (Cpx) crystal from Tullu Moye younger tephra TM-P2 hosting melt inclusions (MI), and inclusions of apatite (Ap) and titanomagnetite (T-Mag). (F) Giano obsidian coulee with undulatory flow banding (dashed line), and alignment of the elongated alkali feldspar (Afs) microcrystals parallel to the flow banding (marked with a dashed line).

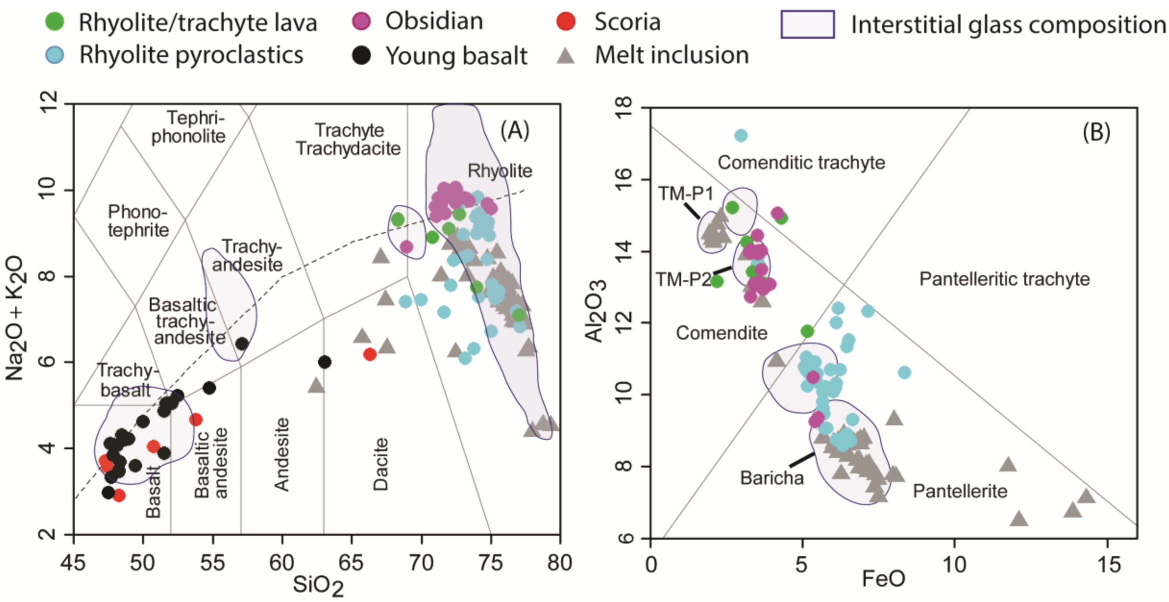

Figure 4: BBTM eruptive products classification diagram based on major element (wt%) whole rock and glass compositions. (A) Total Alkali-Silica diagram after Le Bas et al. (1986). The grey dashed line separates the alkaline and subalkaline series (Irvin and Baragar, 1971). (B) The peralkaline silicic rock classification diagram after Macdonald (1974). The glass composition is indicated by grey fields; some of this data was presented previously by Fontijn et al. (2018) and Tadesse et al. (2022).

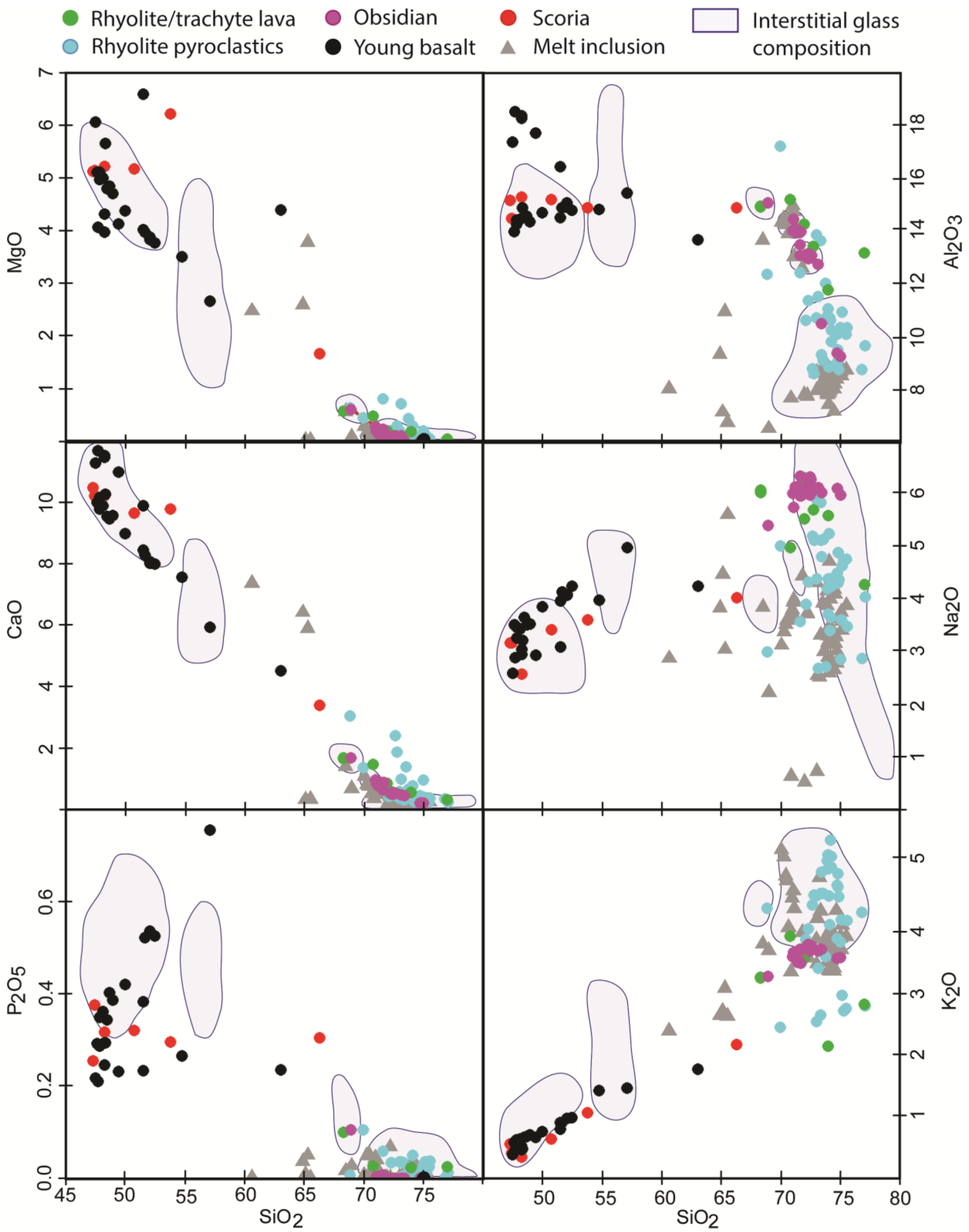

Figure 5: Selected major element (wt%) binary diagrams of the BBTM whole rock and glass compositions.

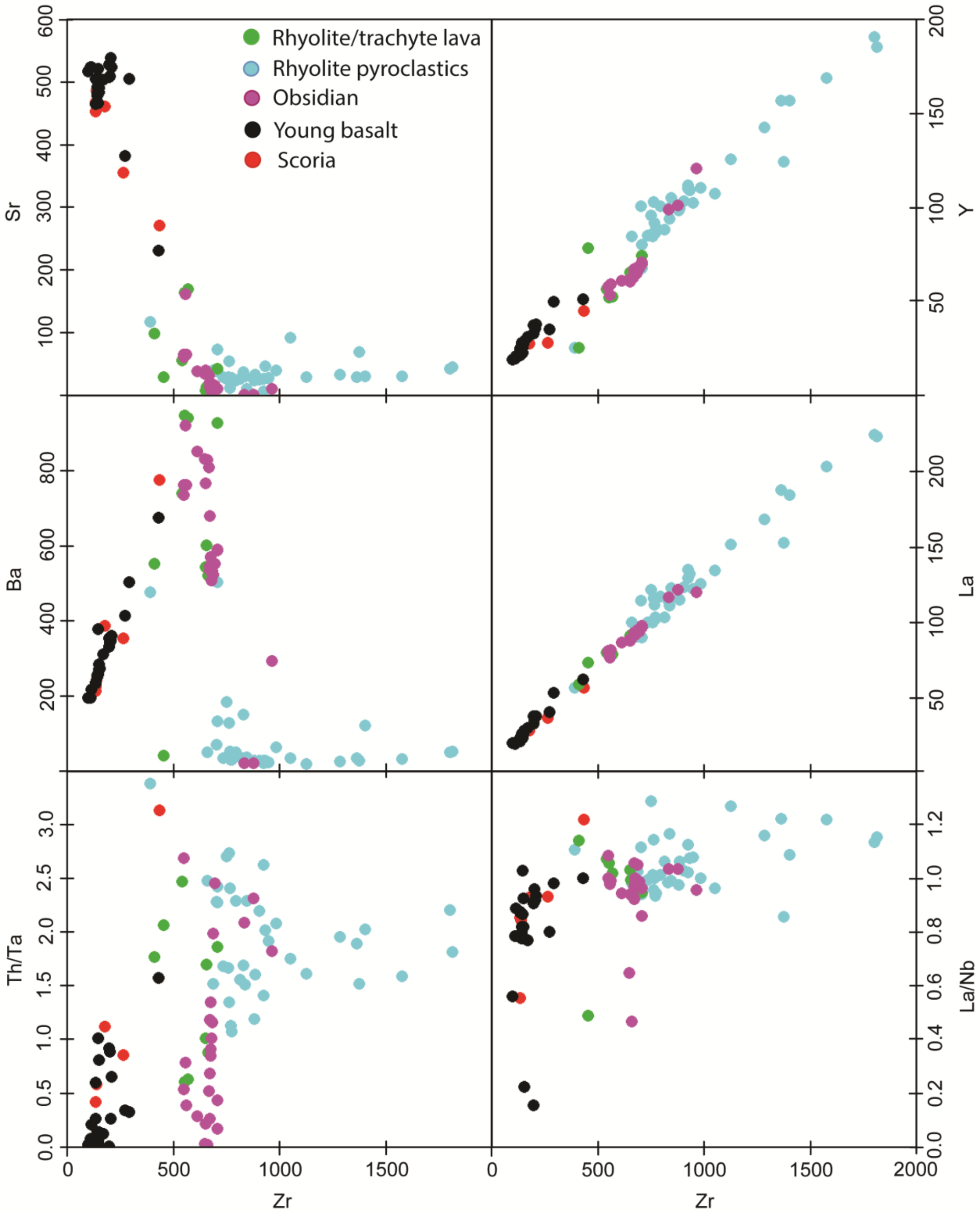

Figure 6: Selected trace element (ppm) binary and ratio plots of the BBTM whole rock compositions.

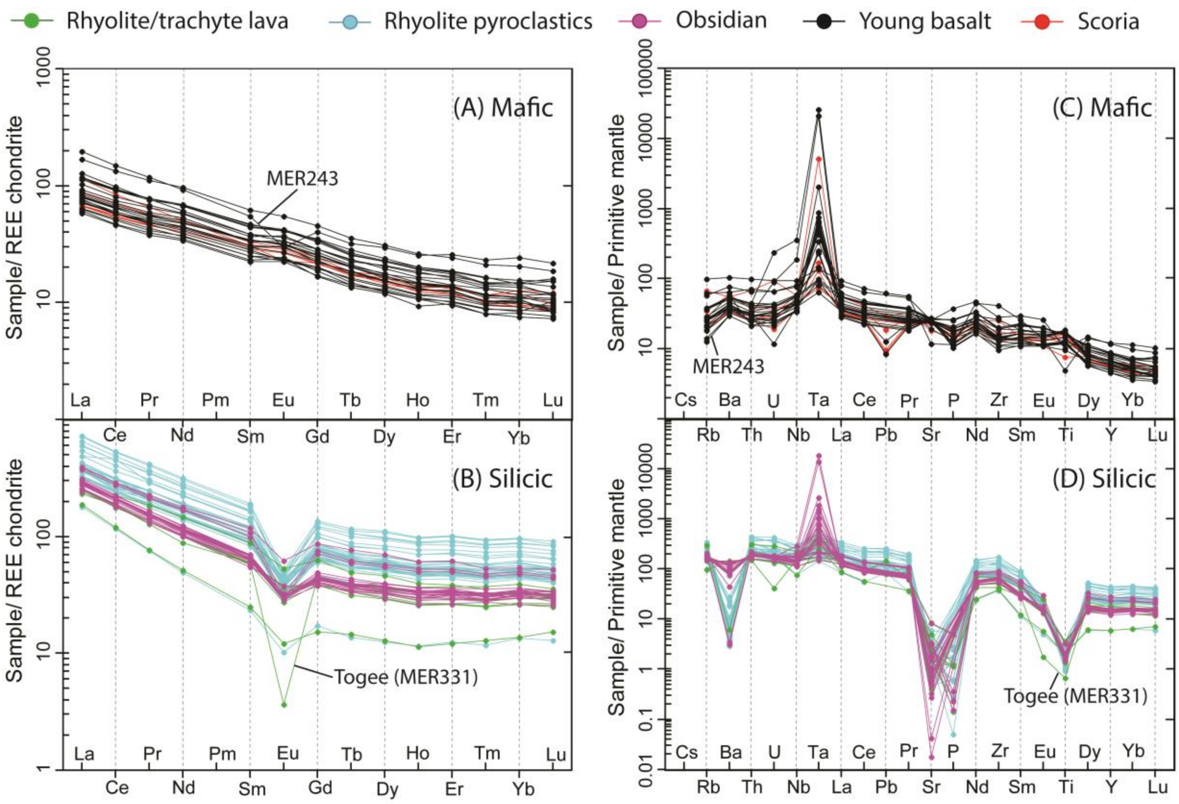

Figure 7: (A) Mafic and (B) silicic BBTM rocks REE variation diagram normalised to chondrite composition (after Boynton, 1984). (C) Mafic and (D) silicic BBTM rocks multi-element spider diagrams normalised to primordial mantle composition (after McDonough and Sun, 1995).

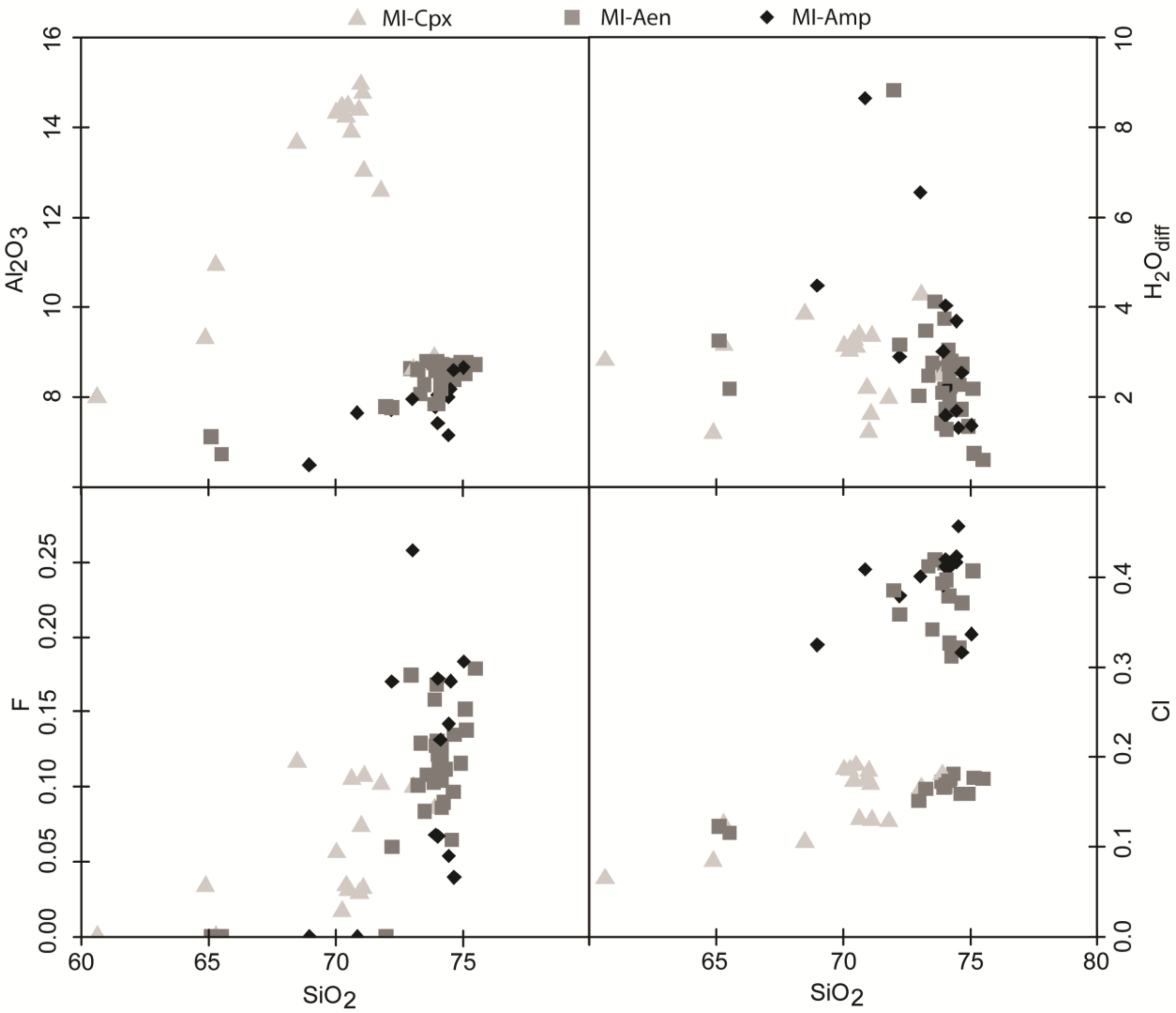

Figure 8: Binary diagrams of the melt inclusion (MI) compositions (wt%) hosted in clinopyroxene (Cpx), amphibole (Amp) and aenigmatite (Aen), with Al_2O_3 and H_2O_{diff}, F and Cl content vs. SiO_2.

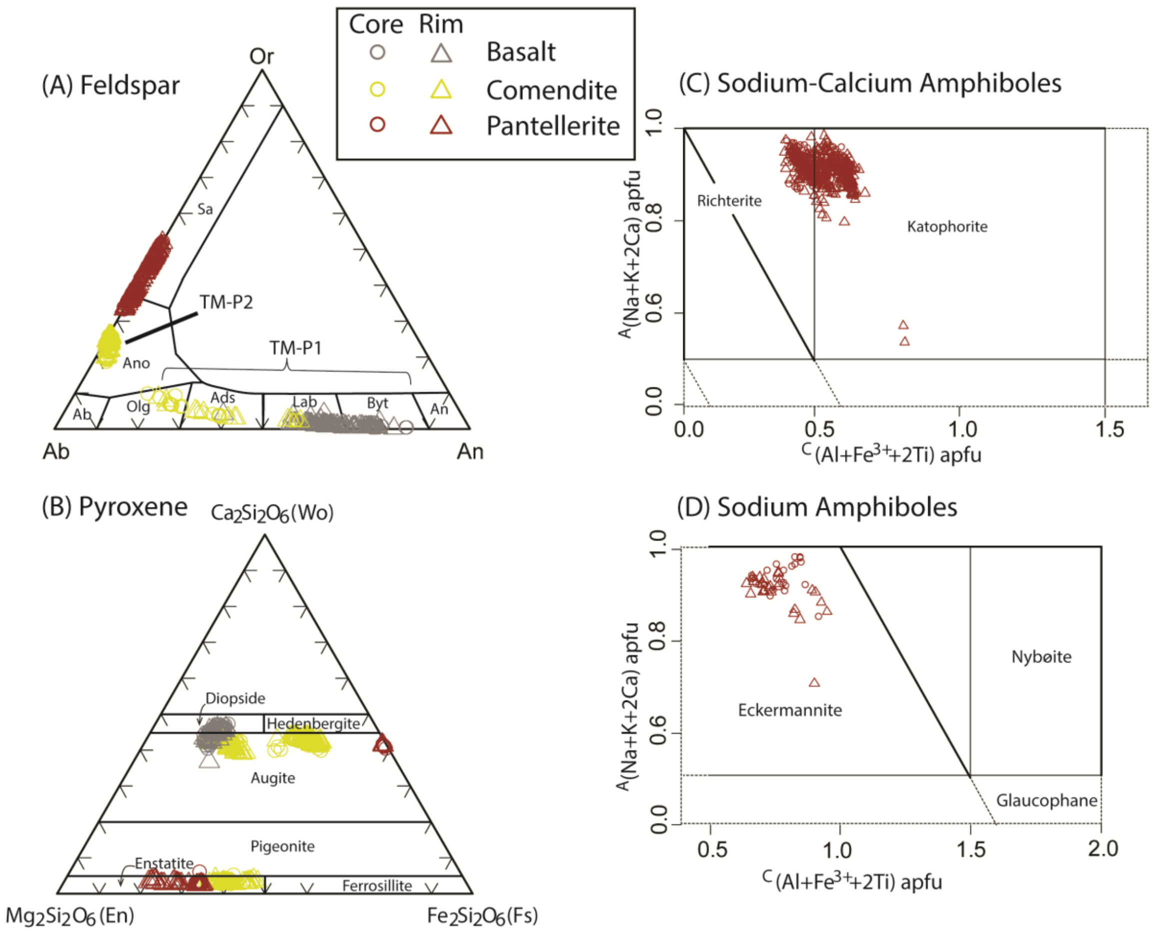

1243

1244 **Figure 9**: Mineral chemistry classification diagrams of (A) feldspar, (B) pyroxene and (C, D)
1245 amphiboles in Qrp and Qwb units, refer SI-3 for more detail. The abbreviations on figure (A)
1246 are Sa (Sanidine), Ano (Anorthoclase), Ab (Albite), Olg (Oligoclase), Ads (Andesine), Lab
1247 (Labradorite), Byt (Bytownite) and An (Anorthite). The pyroxene and amphibole mineral
1248 classifications are from Morimoto et al. (1988) and Hawthorne et al. (2012) respectively.

1249

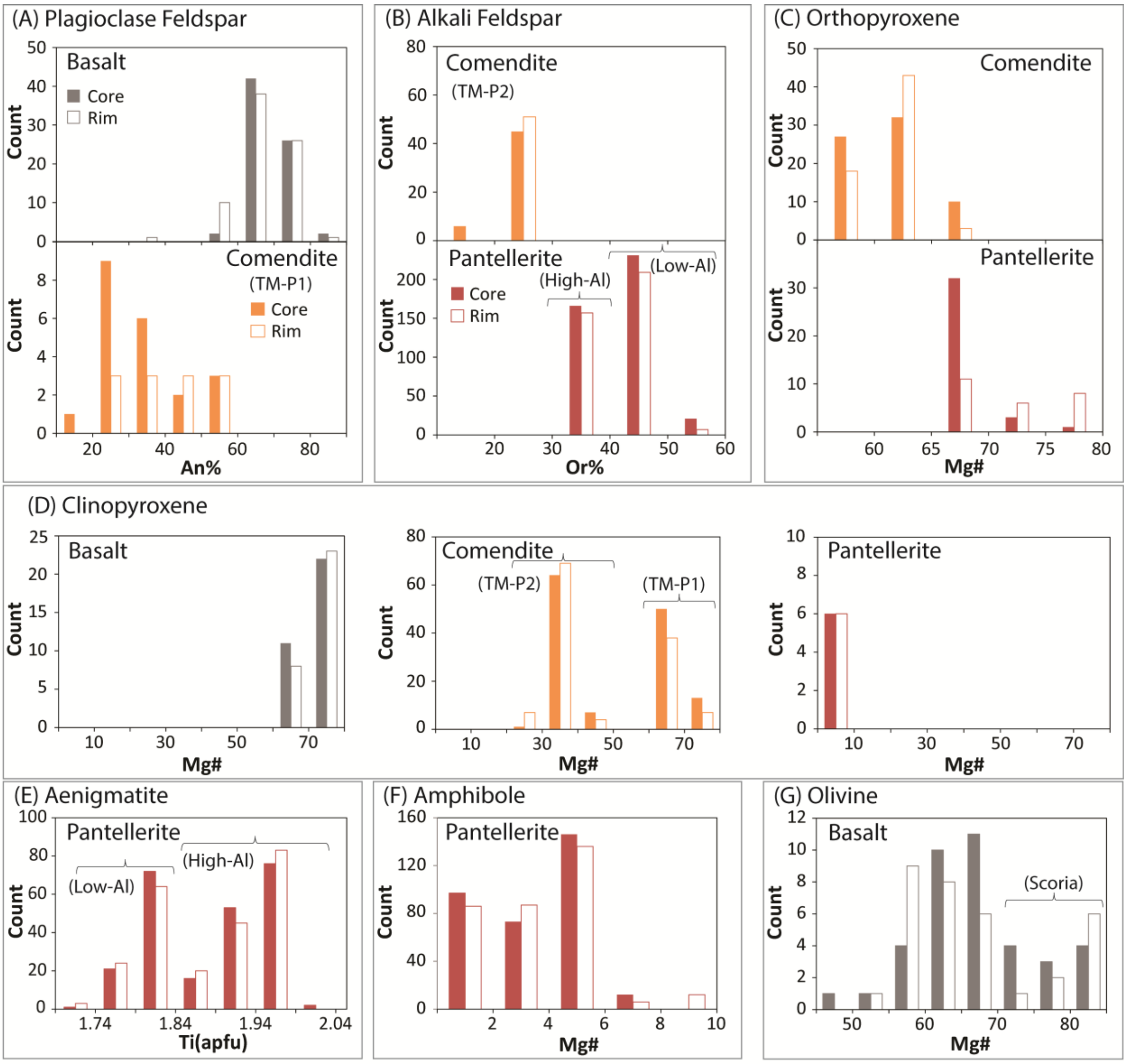

Figure 10: Summary histogram plots of different mineral phases (plagioclase feldspar, alkali feldspar, orthopyroxene, clinopyroxene, aenigmatite, amphibole and olivine) in the BBTM volcanic products. Core and rim analyses result are indicated by colour-filled and empty bars respectively.

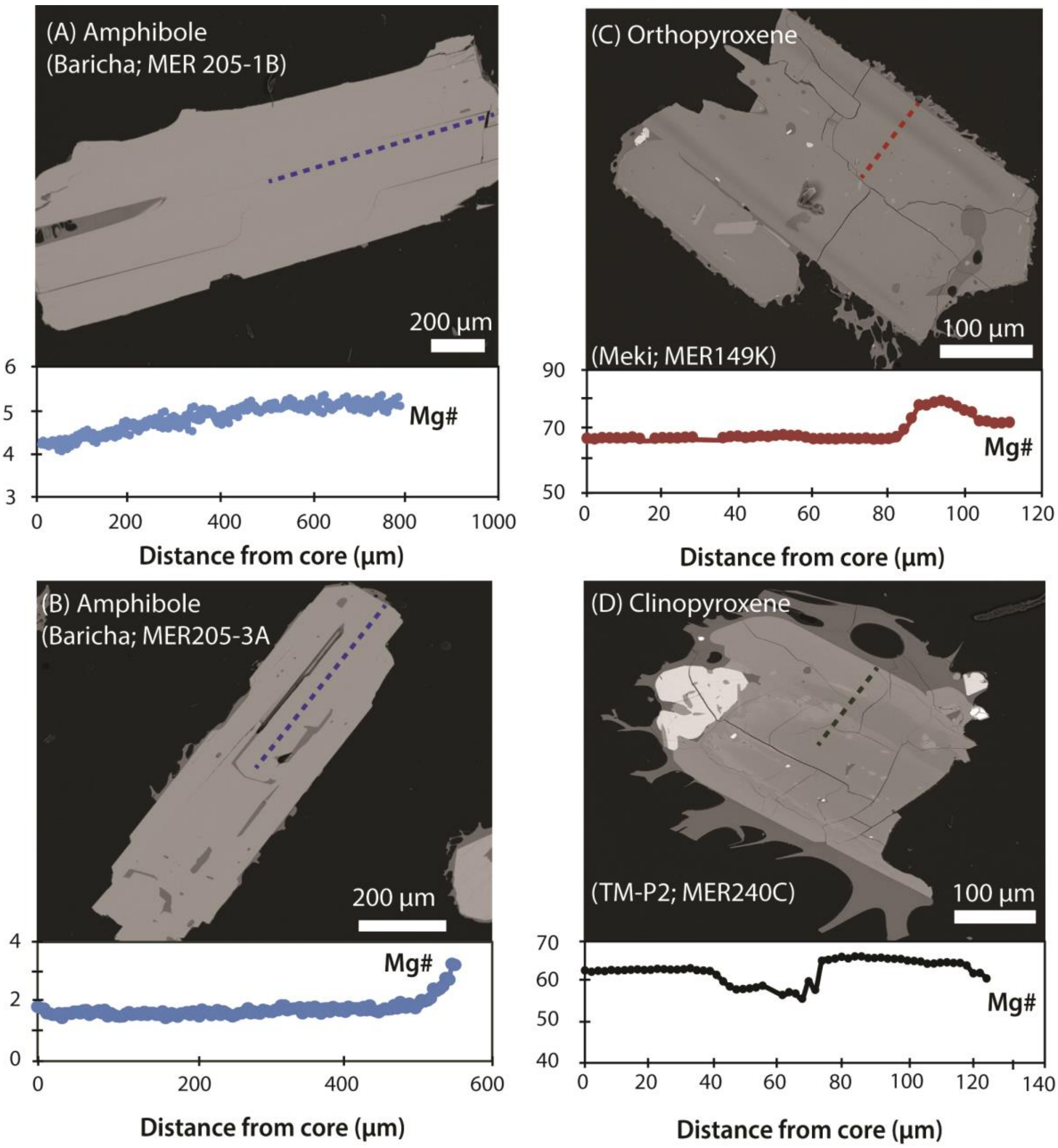

Figure 11: Selected mineral compositional profiles of Mg# and corresponding SEM BSE images on (A, B) amphibole, (C) orthopyroxene and (D) clinopyroxene. Transects are indicated on the image by a dashed line and Mg# is plotted against distance from the core.

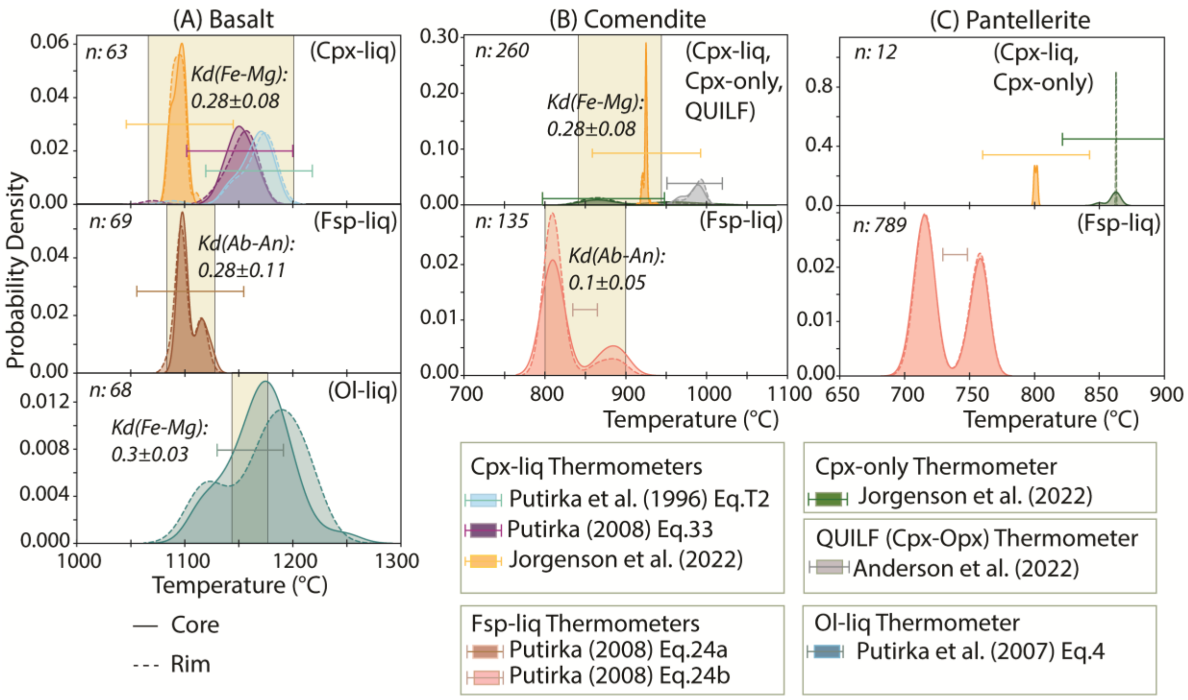

Figure 12: BBTM pre-eruptive temperature kernel density estimate (KDE) plots. The KDE plot bandwidth is 5. (A) Basalt, (B) Comendite and (C) Pantellerite. The extent of chemical equilibrium of the mineral-liquid pairs is indicated by shaded vertical bars for basalt and comendite. The Putirka et al. (2008) experimental dataset to determine the Kd range (i.e., Fe-Mg and Ab-An) for the cpx-liquid and fsp-liquid equilibrium is not calibrated for highly evolved peralkaline (e.g., pantellerite) compositions. Therefore, we based ourselves on textural evidence to evaluate cpx- and fsp-liq equilibrium conditions in the pantelleritic rocks. The standard errors of estimate (SEE) for each equation are indicated by error bars in the figures. n: number of mineral-liquid pairs used for storage temperature calculation.

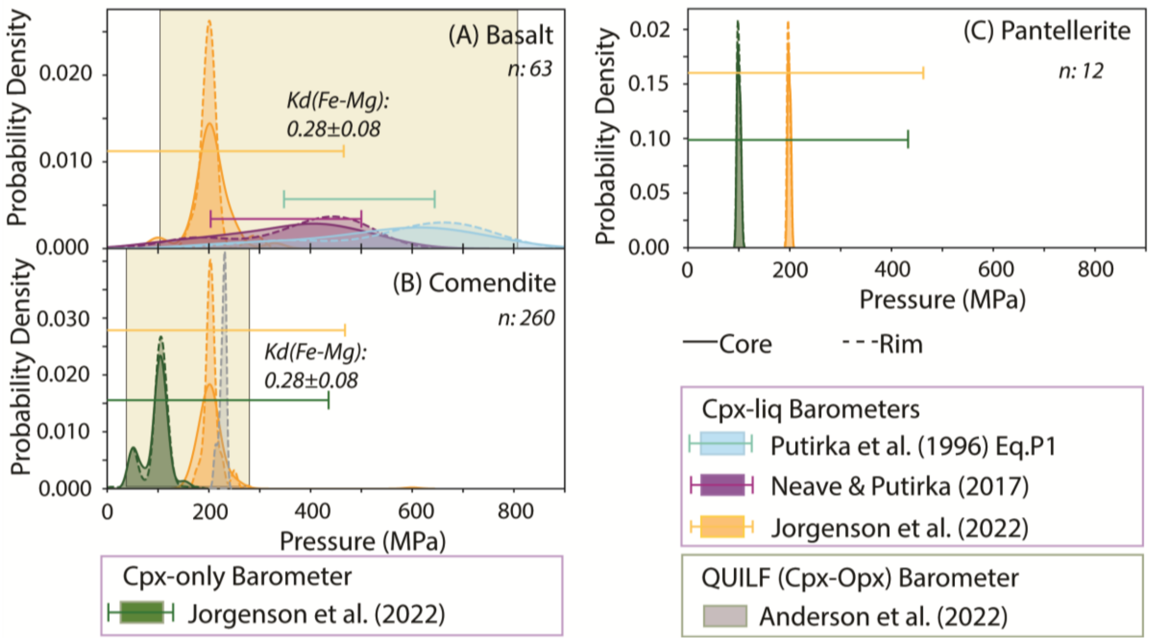

Figure 13: BBTM pre-eruptive storage pressures kernel density estimate (KDE) plots. The KDE plot bandwidth is 0.3. The cpx-liq, cpx-only and QUILF barometers are applied for the (A) basalt, (B) comendite and (C) pantellerite using the different equations indicated in the legend, together with their SEE values indicated by an error bar. The extent of chemical equilibrium of the mineral-liq pairs is indicated by the shaded vertical bars for basalt and comendite. The Putrika et al. (2008) experimental dataset to determine the Kd (Fe-Mg) range for the cpx-liq equilibrium condition is not calibrated for highly evolved peralkaline (e.g., pantellerite) compositions. Therefore, we based ourselves on textural evidence to evaluate cpx-liq equilibrium conditions in the pantelleritic rocks. n: number of mineral-liquid pairs used for storage pressure calculation.

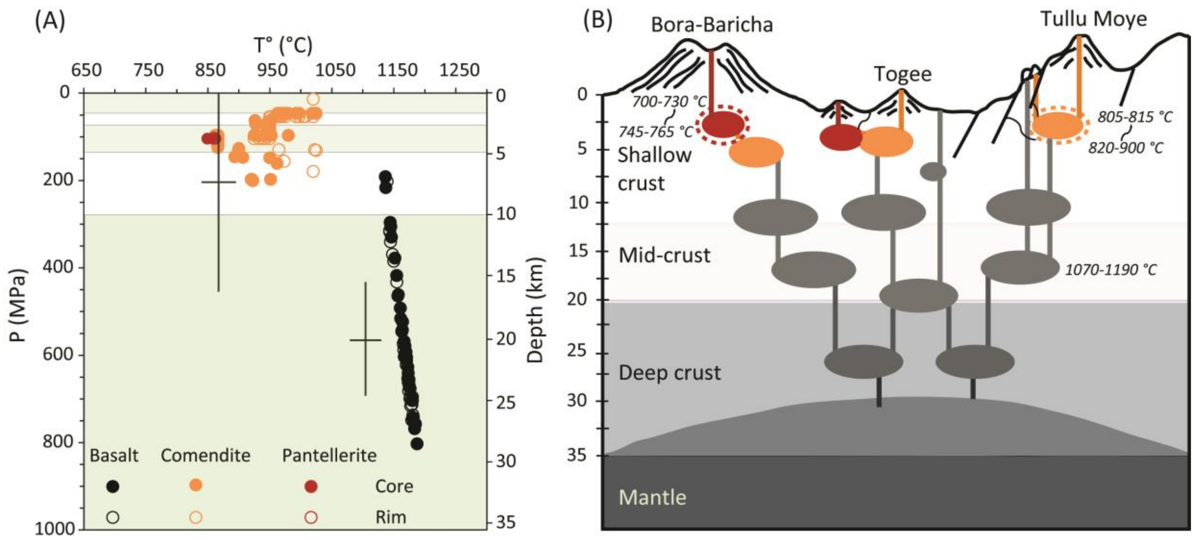

Figure 14: (A) Calculated pressure versus temperature diagram derived from the clinopyroxene geothermobarometers for basalt, comendite and pantellerite compositions. For the basaltic magma, the Putirka et al. (1996) thermobarometer is used, while the Jorgenson et al. (2022) cpx-only thermobarometer is used for the peralkaline magma. The shaded horizontal regions show the depth levels of high conductivity from magnetotelluric surveys (Samrock et al., 2018). Crosses indicate the error bars of the geothermobarometers. (B) Conceptual model for the BBTM magma plumbing system. Colour is cross-correlated to the legend on panel (A). The progressive temporal storage temperature changes of pre-existing reservoirs at shallow crustal levels are indicated by dashed lines. The storage temperature values presented on this diagram are calculated based on the fsp-liq thermometers of Putirka et al. (1996) and Putirka (2008).

Supplementary Information

Supplementary Information 1 (SI-1): BBTM representative bulk rock major and trace element dataset analysed by ICP-OES and ICP-MS respectively. Geological units and geographic coordinates (Latitude – Longitude, WGS84) are also given. The whole rock data presented here in the supplementary information is not normalised. <bld: analysis below the detection limit. na: not analysed.

Supplementary Information 2 (SI-2): BBTM pyroclastics products glass major element dataset analysed by EPMA. The glass chemistry data presented here in the supplementary information is not normalised.

Supplementary Information 3 (SI-3): Mineral chemistry and melt inclusions dataset analysed by EPMA.

Supplementary Information 4 (SI-4): Various selected figures elucidating BBTM eruptive products bulk rock major and trace element composition, glass and mineral composition.

- **Figure SI-4-1**: LOI (Loss of Ignition) against Na_2O and Al_2O_3 bivariate plot.
- **Figure SI-4-2**: Selected major elements against SiO_2 binary plots.
- **Figure SI-4-3**: Selected trace elements against Zr binary plots.
- **Figure SI-4-4**: Fe-Ti oxides composition classification, binary and histogram plots.
- **Figure SI-4-5**: SEM back scatter electron (BSE) image of (A) alkali feldspar, (B) clinopyroxene, (C) aenigmatite and (D) titano-magnetite hosted in plagioclase feldspar.

Supplementary Information 5 (SI-5): Pressure and temperature estimation dataset retrieved by different geothermobarometers. The performance test results of the cpx- and fsp-associated thermo(baro)meters are also presented.

Table 1: Synoptic overview of the different magma type compositions and pre-eruptive storage conditions in the BBTM volcanic system. Stratigraphic sequences are after Tadesse et al. (2022). The storage pressures for the peralkaline magma (comendite and pantellerite) have a high peak at 100 MPa as shown on the KDE plot (Fig. 13).

Magma Type	**Geological unit**	**Stratigraphy Sequence**	**Bulk composition**	**Pre-eruptive storage conditions**		
				Temperature (°C)	Pressure (MPa)	Depth (Km)
Basaltic	Qwb		Basaltic (49.6 ± 2 wt% SiO_2)	1070-1190	200-800	7-29
TM-P1 comendite	Qrt, Qrp & Qoc	TM-P1	Comenditic (72 ± 2 wt% SiO_2)	820-900	0-175	0-6.3
TM-P2 comendite	Qrt, Qrp & Qoc	TM-P2		805-815	175-210	6.3-7.5
High-Al pantellerite	Qrt & Qrp	Meki, Bora, Oda, Werdi & Pumice cones	Pantelleritic (73.8 ± 1.5 wt% SiO_2)	745-765	100	3.6
Low-Al pantellerite	Qrt & Qrp	Baricha		700-765	100	3.6